Final Report to the

National Aeronautics and Space Administration

on

Global Failure Modes in Composite Structures

NASA Grant NAG 1-1975

Prof. W.G. Knauss
Luis Gonzalez

California Institute of Technology
Pasadena, California

July 2001

INTRODUCTION

Background

Composite materials provide well-known advantages for space and aeronautical applications in terms of strength and rigidity to weight ratios and other mechanical properties. As a consequence, their use has experienced a constant increase in the past decades and it is anticipated that this trend will be maintained in the near future. At the same time, being these materials relatively new compared to metals, and having failure characteristics completely different from them, their damage growth and their failure mechanisms are not as well understood in a predictive sense. For example, while in metals fracture produces "clean" cracks with their well defined analytically stress fields at the crack tip, composite fracture is a more complex phenomenon. Instead of a crack, we confront a "damage zone" that may include fiber breakage, fiber micro-buckling, fiber pullout, matrix cracking, delamination, debonding or any combination of all these different mechanisms. These phenomena are prevalent in any failure process through an aircraft structure, whether one addresses a global failure such as the ripping of a fuselage or wing section, or whether one is concerned with the failure initiation near a thickness change at stringers or other reinforcement. Thus the topic that has been under consideration has wide application in any real structure and is considered an essential contribution to the predictive failure analysis capability for aircraft containing composite components.

The heterogeneity and the anisotropy of composites are not only advantageous but essential characteristics, yet these same features provide complex stress fields, especially in the presence of geometrical discontinuities such as notches, holes or cut-outs or structural elements such as stiffeners, stringers, etc. To properly address the interaction between a damage/crack front and a hole with a stringer it is imperative that the stress and deformation fields of the former be (sufficiently well) characterized.

The question of "scaling" is an essential concern in any structural materials investigation. For example, experiments in the past have shown that the "strength" of a composite depends on hole size. As a consequence the validity of traditional fracture mechanics concepts applied to composite materials failure must be questioned. The size of the fibers, the dimensions of the laminae, etc. together with the fact that, because of the layered anisotropy, the stress field is no longer two-dimensional, prevent the otherwise obviously confident use of "similarity concepts". Therefore, the question needs to be raised of whether in composites "size matters or not", *i.e.*, whether the results obtained in a laboratory using small coupons are truly representative of the situation involving a full scale component.

Scope of the work

This document reports on two efforts, both concerned with failure initiation and progression at thickness discontinuities in structures of composite materials. The first study, which is basically completed and documented in the published literature addressed failure initiation at a step in ply-lay-ups, accounting for three different configurations in that lay-up. Rather than recount these results here, this work is summarized in the form of three publications at the end of this report. Inasmuch as that presentation is fairly complete, there is no need for further explanations at this point, except with respect to one of these three publications. This paper arose as part of the study of time dependent response of composites under long-term use. A typical question arising in the characterization of time-dependent materials, namely how the loading history affects the time-related properties measurement. This paper documents an efficient way to maximize the information gathered in a standard laboratory test designed to measure material relaxation on standard test facilities.

Accordingly, we separate this report into two portions, Phases I and II, though not in chronological order so that Phase I thus recounts the most recent (and ongoing) efforts, with the complete description of past work relegated to Phase II a the end of the report.

The problem of concern in the ongoing study (Phase I) is the determination and characterization of the onset and progression of structural failure in laminated composite materials by the growth of a crack-like feature, with special interest centered on the role of relative scaling and in the influence of geometric discontinuities, representative of structural elements such as stringers or stiffeners (Fig. 1).

Typically, fuselages, spacecraft shells, launcher fairings as well as pressure vessels, which can be found in many aerospace structures and more earthbound applications, consist of a shell reinforced with stringers, ribs or some kind of tear straps. These reinforcements are typically bonded or co-cured elements. When damage is introduced into the structure, a situation analogous to that depicted in Fig. 1 occurs. To explain how the damage develops, the path it will follow or whether and under what conditions it will be arrested in the presence of a stiffener was one of the principal objectives in this investigation. Certainly that information is needed in order to be able to implement design methodologies and criteria for the utilization of composite materials to their full potential.

PHASE I

Global Failure/Fracture Instabilities

Composite materials derive many of their advantages from their anisotropy, but it is also well known that this feature gives rise to complicated three-dimensional states of stress in the presence of geometrical discontinuities such as cutouts, notches or ruptures (that could have been produced by penetration, for example). A further factor that renders failure description of composites more complex than that for traditional engineering materials is precisely their distinctive heterogeneity, i.e., the composite is an aggregate of unidirectional plies which in turn are composed of different phases, namely the matrix and the fibers. Thus when a global failure occurs, the propagation of any damage occurs through a mechanism that is only ***similar*** to a crack in global sense.

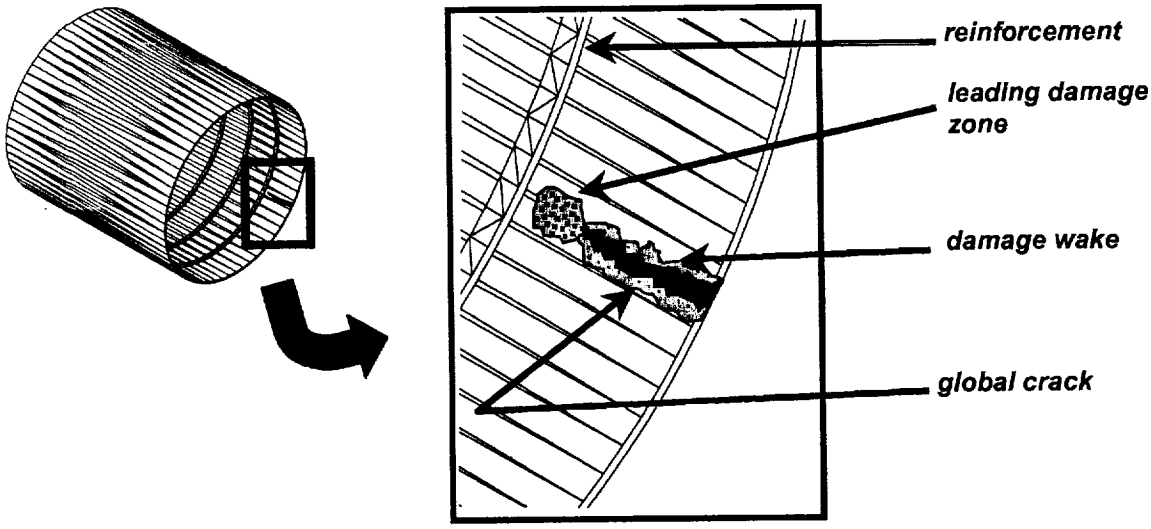

Figure 1. A "Global Crack" traversing a built-up structure with damage wake and interaction zone near a reinforcement element.

In detail, the failure progression has features of a band or region of damage rather than of a well-defined, classical crack-like geometry, but seen from a proper large

or global scale such damage progression may be treatable by a crack analysis. This situation is represented schematically in Figure 1, where a "crack-like feature" (not sharply defined by flank boundaries) tracks through an extended damage zone which represents a multitude of local or small scale damage phenomena, including matrix cracking, fiber pull-out, delamination, and various forms of fiber fracture.

Such a macro-crack phenomenon has consequences when it interacts with other components of a structure, in that the details of the interaction do become important. Specifically, the issue here is that of the raising of stress levels at skin-structure joints that derive from an approaching macro-crack. This latter feature is likely to have a rather broad "front" with a diffuse but distinct stress concentration capability. Since such a front probably involves ply separations and fractures, this zone could extend on the order of inches. It is, therefore, very important to assess the size of such a zone for computational and design purposes.

It is doubtful that this particular or other structural size parameter (e.g. width of the wake, interaction zone near a reinforcement) could be established uniquely in the laboratory by using only small (structural) specimens. Rather, (nearly) full-scale simulations would be necessary to be conducted for this purpose to be able to determine, out of the combined results, the scale factors for these failure modes. The test facilities at Caltech impose a limit on the size of the specimens that could be tested but, nevertheless, elements close to working panels fell within these limits.

Specimens of the geometry illustrated in Figure 2 permit us to understand how a macro crack interacts with a stringer. Clearly, the stiffness of the stringer determines the range over which the forces at the "tip" of the global crack are distributed and abated near the stringer; consequently the failure may stop (temporarily?). The (possible) stress abatement with approach to the stringer depends on the (tensile and bending) stiffness of the latter, and probably on their relative values compared to those of the fracturing plate. These dependencies need yet to be worked out.

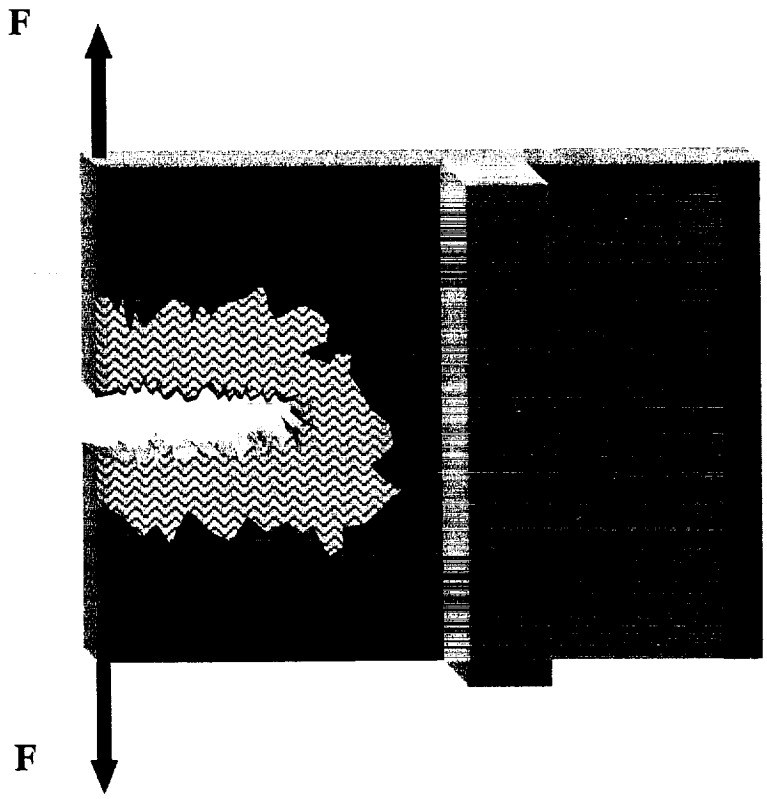

Figure 2. Exemplar configuration of a global crack traversing a reinforced plate.

An initial analysis demonstrated that to understand the interaction of the crack with the stiffener, the nature of the stress and strain fields (which are determined by the internal damage) in a sheet as a global crack propagates through it needs to be addressed. It was indeed surprising to us that very little work had been done on this topic. Thus, leaving the crack-stiffener interaction for future work, for which this study will serve as a foundation, its main topic has been the detailed description of the failure process, the accurate measurement of the stress/strain fields in the vicinity of the "crack tip", the quantification of the extension of the "zone of 'crack' influence" and to examine this for different lay-ups.

To quantify scale effects it is necessary to conduct tests on differently sized specimens, namely from a coupon size to the largest specimens which the testing

facilities at Caltech can accommodate (roughly 18 × 18 in). The number of ply configurations is nearly limitless, however, a set of typical results should suffice for assessing the important variations for analysis and design purposes, once extrapolations on such data have become better understood.

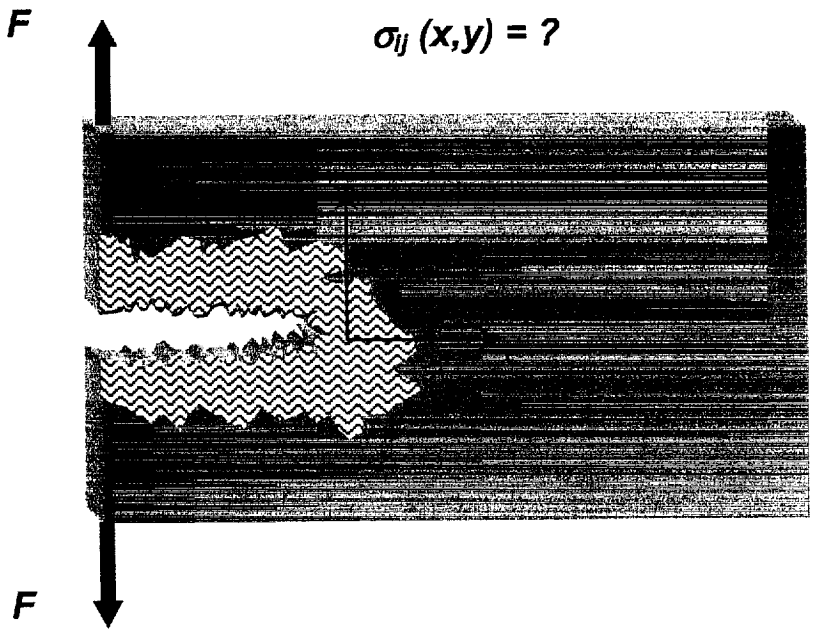

Figure 3. Examination area at the front of a fracture zone in a composite (unreinforced) plate.

Summary of work accomplished in Phase I

The purpose of this study has been to analyze and characterize the failure and "fracture" mechanisms of laminated composite materials in terms of typical structural load descriptions rather than in terms of micro-mechanics considerations, such that the emphasis on **structural design** criteria dominates the investigation. To understand, predict, avoid and control these processes, clear and effective criteria need to be developed based on sound physical principles. Later on, these criteria can be incorporated into numerical or computational analyses.

To achieve that aim, accurate measurements of the deformation and strain fields that the material undergoes while subjected to loading are needed; particularly in the region around the "crack tip" or "failure front". The Digital Image Correlation method (DIC) has been chosen to provide "field" measurements of those deformations from which the strains can be calculated. Other measuring techniques such as the use of strain gages or optical methods, such as Moiré and Moiré interferometry were considered and studied but DIC was the preferred one because it appeared to offer certain advantages in terms of accuracy and simplicity of the setup.

The DIC method provides surface information but nothing is said of the state of the interior of the material (state of stress or damage). For determining the stress in the plate interior finite element analysis was employed, using the surface measurements as input. In addition, x-ray imaging aided in the monitoring of the extent of damage within the plate.

To study the influence of "scaling", three sets of specimens were manufactures (at LaRC), starting with panels of "coupon" size (6 × 6 in), another of intermediate dimension (12 × 12 in) and, finally, a set of panels of roughly "component" size (18 × 18 in). Taking advantage of the fact that the panels are not quasi-isotropic, it was possible to study the influence of the lay up by cutting the slits along or perpendicular to the 0^o axis of the material.

The tests on the smaller panels were conducted on an Instron screw-driven tension testing machine but it proved to have insufficient load capability for the testing of the medium and larger panels. For that task we turned to an MTS servo-hydraulic system rated at 250 kN.

Digital Image Correlation (DIC)

As has already been mentioned, the DIC method allows the accurate measurement of displacement fields on a planar deforming solid. Two of its main advantages are that it provides field measurements, as opposed to point ones, and that it is non-intrusive.

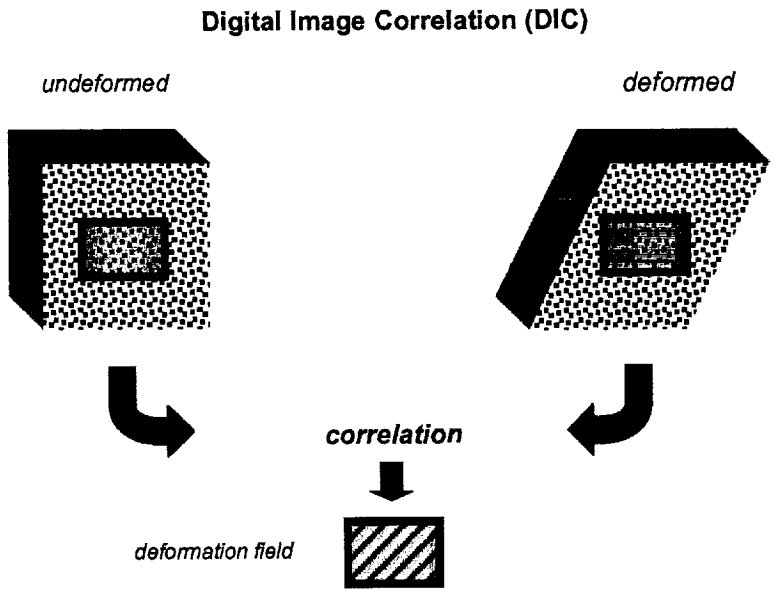

Figure 4. Schematic description of the digital image correlation method. Two digital photographs of the same area (in the undeformed and in the deformed state) are compared to produce a mapping of the deformation field.

Digital Image Correlation is a computer vision method that extracts whole-field displacement data by comparing the features in a pair of digital images of a specimen surface acquired before and after deformation. More specifically, the physical problem of measuring in-plane displacements at a grid point on a macroscopically flat surface can be formulated as a correspondence mathematical issue of minimizing a correlation

function over a subset image region containing the grid point with respect to six coefficients, namely, the two in-plane displacement components u and v, and their four derivatives u_X, u_Y, v_X and v_Y, all evaluated at the grid point. As the specimen is displaced during a test, images are taken at prescribed intervals and ultimately reduced to a grayscale and saved as raw data files brightness values. When the test is complete, it is the purpose of the DIC software to track the brightness values from image to image and report the in-plane displacements due to translation, rotation, extension, and shear. These, of course, form the two dimensional whole field displacement and strain maps for the specimen an can be reported cumulatively or incrementally.

Several implementations of the DIC method have been demonstrated in a range of experimental mechanics and materials applications (Sutton et al., 1983; Chu et al., 1985; James et al., 1990; Franke *et al.* 1991; Vendroux and Knauss, 1994, 1998; Choi and Shah, 1997; Tong, 1998; Li *et al.*, 1998). For the present work, the code developed by Vendroux and Knauss has been used.

The specimens used in this study did not naturally present surface features that could be used for DIC and thus it proved necessary to provide a spot or splatter pattern of white and black paint on the area of interest. An example of this is shown in Fig. 5.

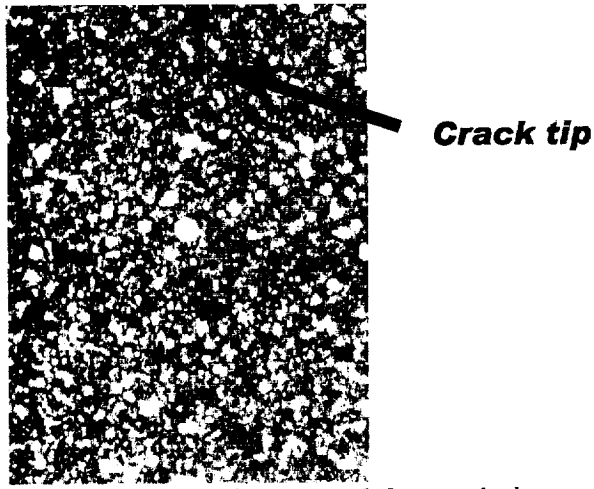

Figure 5. Photograph of the region around the crack tip with spot pattern used for digital image correlation.

To test the applicability, accuracy and limitations of this method, a series of tests were performed. All of them consisted in the measurement of a known strain field via DIC by subjecting strips 1" wide of polycarbonate and aluminum (5052 alloy) to uniform uniaxial tension, as depicted in Fig. 6. The strains derived with the aid of DIC were compared to those measured with a strain gage. The gage section shows the speckle pattern used for the DIC.

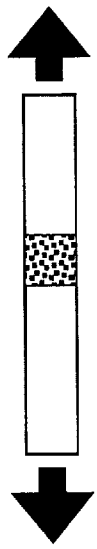

Figure 6. Tension specimen with speckle pattern at gage section for digital image correlation.

The aluminum specimens were not of much quantitative use because they deformed plastically along shear bands and this localized deformation rendered the strain gage measurements non-informative if not meaningless. Nevertheless, qualitatively, those tests showed that measurements were on the right track since the shear bands clearly appeared in the deformation field plots, as can be seen in Fig. 7.

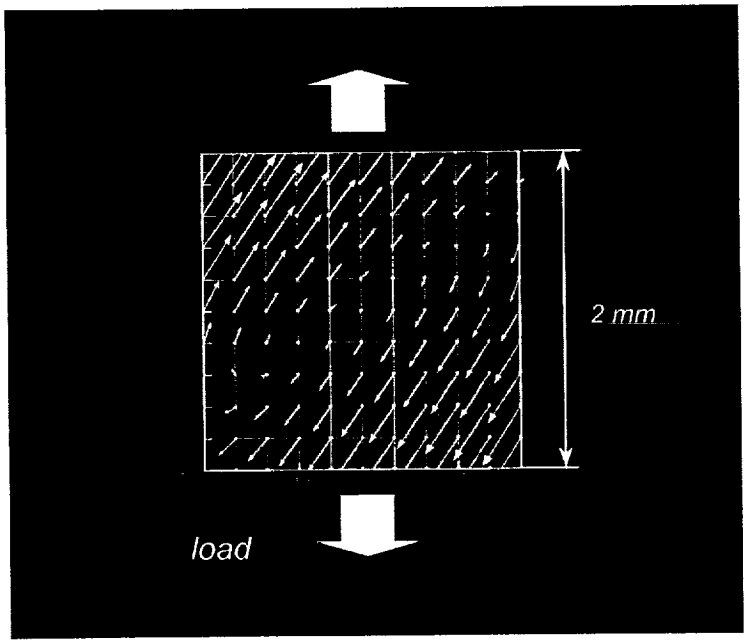

Figure 7. Deformation field of a 5052 Aluminum specimen under uniaxial tension. The shear bands at 45° are clearly distinguishable.

This time the information was presented in the form of a vector plot. This information is useful in the context of later experimental efforts that involve inhomogeneous deformations such as the front of a fracture profile. Thus, for the calibration purposes, polycarbonate was used instead of aluminum. The test described in Fig. 6. was repeated several times and plots of the deformation field similar to that shown in Fig. 8 were obtained.

Once the deformation field is known, the strains can be computed. The average for the whole region was computed and compared to the measurements obtained with the strain gage. The two values are presented in Fig. 9. Superimposed is a straight line of unit slope which is where the points should fall. It can be seen that the values have a

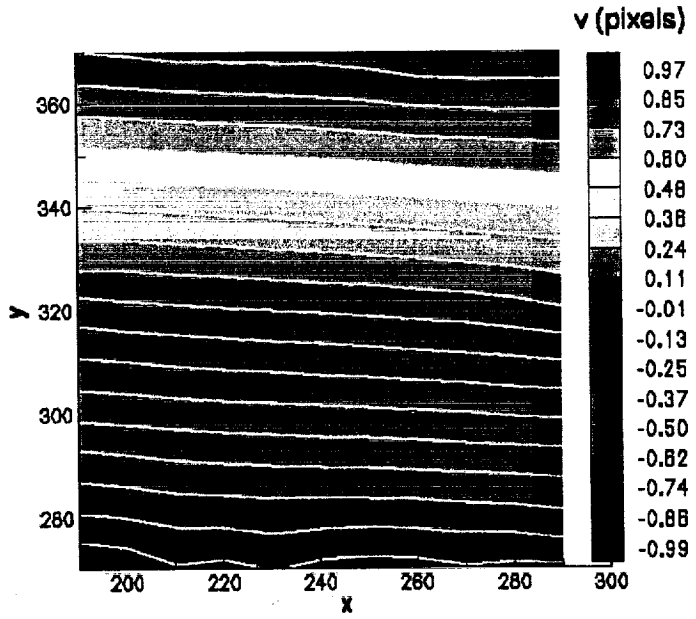

Figure 8. Deformation field calculated through digital image correlation for a policarbonate specimen (the area plotted is about 0.045" × 0.045").

good agreement and that the values for the error cited in the literature of 0.1 % of strain are correct. Thus, these tests supported the claim for the use of the DIC method in the measurement of the strain fields of the region around the "crack" front.

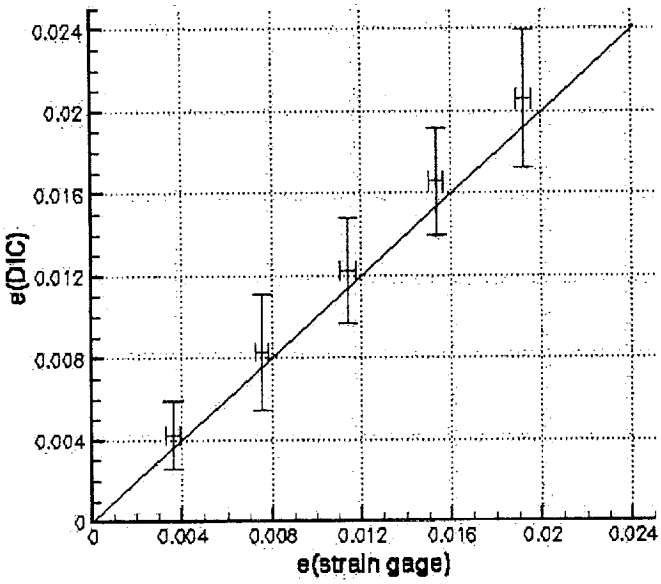

Figure 9. Comparison between strains calculated via digital image correlation and measured with strain gage for a polycarbonate specimen.

X-ray inspection

X-ray radiography is one of the most efficient nondestructive evaluation (NDE) techniques in use. Its basic principle consists of transmitting x-rays through the part to be examined. The transmitted energy is captured on a photographic film placed directly behind the opposite surface. Defects or flaws in the material produce a variation in energy transmission that shows up as shadow images on the photographic film.

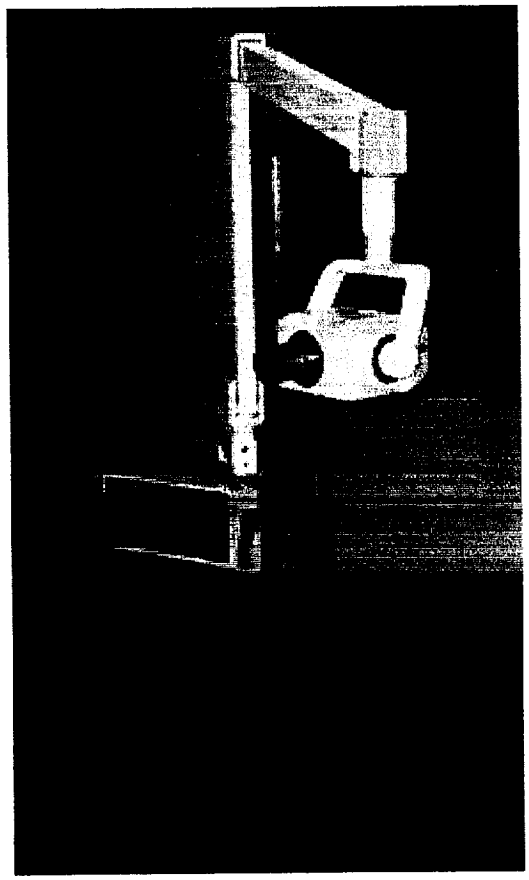

Figure 10. X-radiography station built at Caltech to observe the interior of the test specimens while undergoing loading.

Planar defects normal to the radiation beam, such as delaminations or interlaminar cracks, are not detected by radiography unless a radio-opaque penetrant is first injected into these defect areas to improve the contrast. This technique, called penetrant-enhanced x-ray radiography (PEXR), is often used to detect delaminations caused by low energy impacts; however, its use requires a way for the penetrant to access the defect areas and is therefore limited to delaminations that are open to the surface. Several penetrants, including zinc iodide, silver nitrate, trichloroethylene, diiodomethane (DIM), diiodobutane (DIB), and tetrabromoethane (TBE), have been used for PEXR.

In our work TBE, DIM and DIB were used. The articles in the literature that deal with PEXR cite them extensively because of their excellent penetrant and x-ray absorption or contrasting capabilities.

The first tests were performed with TBE which later on was substituted by DIM because of the former's toxicity, corrosiveness and also to the fact that it would wash away the paint used for the spot pattern of the DIC method. The DIM provides results just as satisfactory without all the inconveniences of TBE.

The film utilized was 4 × 5 in. sheets of Kodak Professional TMAX 100. Tests recommended an exposure time of 4 seconds in order to achieve the best contrast. For an x-ray generator, we searched for and acquired an x-ray machine formerly used for dental applications (Fig. 9), a Yoshida X-70 unit, with a 70 kVp source Its exposure times and its voltage range fall precisely in the area of our needs and at an affordable price.

Since this machine was not new, we had to refurbish it and condition. Besides, since it has been designed for wall mounting, we needed to modify it in order to mount it on a mobile stand that can be translated and located next to the loading devices, i.e. the MTS or INSTRON machines. This is significant since it would allow us to obtain the x-

ray images without having to dismount (and unload) the specimens, and therefore permit us to follow the damage progression.

Specimens

The test specimens were designed bearing in mind all the information so far explained. They were fabricated at the NASA Langley Research Center after substantial delays. The material combination used was IM7 / PETI-5 the main properties of which (per lamina) are summarized in Table 1.

Table 1. Properties (per lamina) of IM7 / PETI-5 as fabricated.

E_1 = 22.25 msi (in tension)
E_2 = 1.16 msi (in tension)
E_1 = 20.35 msi (in compression)
E_2 = 1.16 msi (in compression)
ν_{12} = 0.29
G_{12} = 0.61 msi
α_1 = -0.14 micro in/in/° F
α_2 = 16.85 micro in/in/° F
α_{12} = 0.00
t = 0.0055 in
ρ = 0.0574 lb/in^3
V_f = 57.39 %

The lay-up was chosen to represent a generic configuration representative of a typical aero-application such as an airplane fuselage, and one that would not be quasi-isotropic so as to be able to study the influence of the change of orientation on the "fracture properties". Thus, the panels were fabricated with the following lay-up, $[90_2, +45_2, 0_2, -45_2, 0_2, +45_2, 0_2, -45_2]_S$. Accordingly, the nominal thickness was 0.176 in.

From these panels compact tension specimens were cut in three different sizes according to the diagram of Fig. 11. Half of the specimens were cut with the notch along the 0^o and the rest at a right angle to it. This allowed testing samples where there was a dominance of 0^o plies and, accordingly, specimens where the 90^o layers were the most abundant.

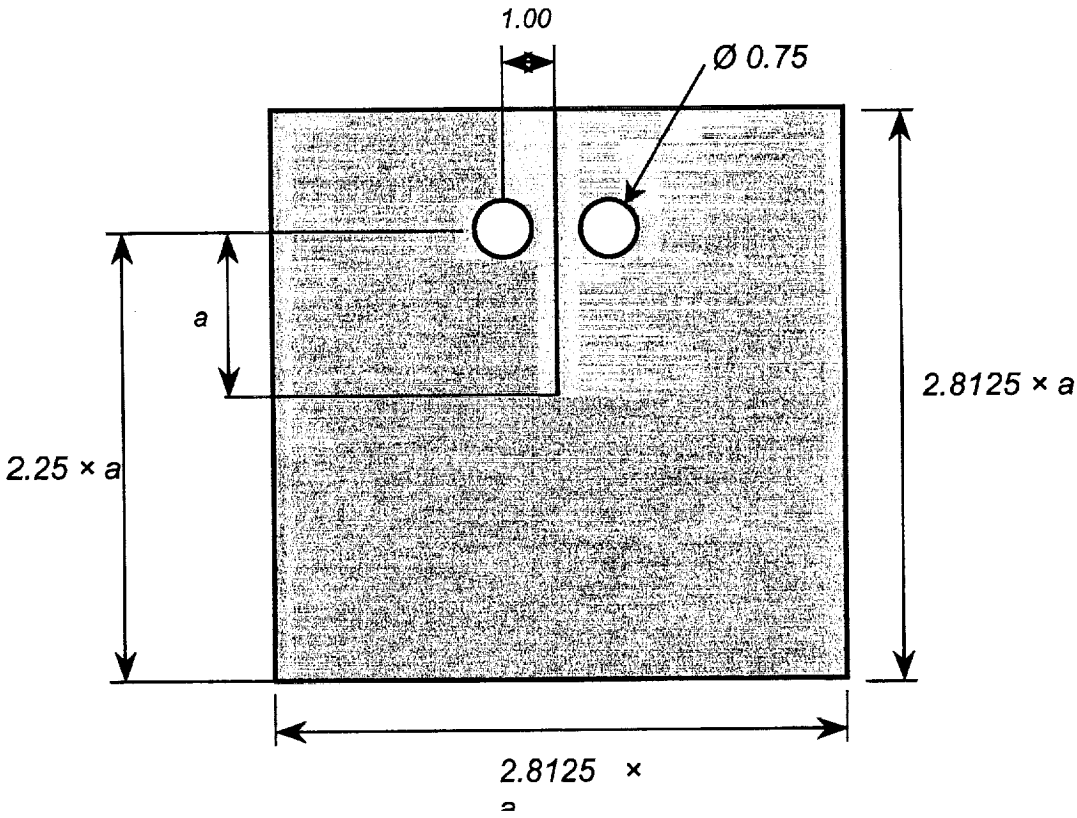

Figure 11. Specimen geometry. a = 2.16, 4.32 and 6.48 in for the small, medium and large specimens, respectively.

We remind the reader that our main interest is in the naturally formed conditions at the tip of an advancing fracture. However, to get a fracture started, an initial crack-type configuration needed to be imposed. The notches or slits were needed to be as thin as possible and, as can be observed on Fig. 11, they would result in very long cuts, especially for the largest panels. These long slits cannot be produced with conventional saws because since they would be very thin and the material is tough and hard, the tool would tend to wobble and not produce a straight cut. Besides, the minimum gage that can be obtained by saws would be unacceptably large.

Different options were studied. Laser cuts appeared as an attractive solution but after several tests were performed on some scratch material, this method had to be discarded. The high temperature and the high-pressure gas used for the process made that the material would bulge on the exit side and burst. EDM, a technique normally used for producing extremely thin cuts and difficult patterns in metals, was not applicable because of the low conductivity of the composite material.

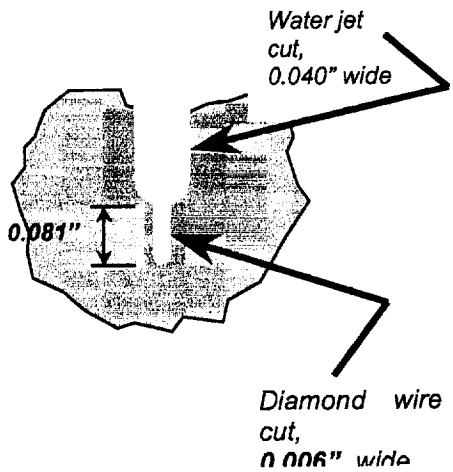

Figure 12. "Crack" tip detail. The main cut of the slits was produced by water jet process and then extended with diamond-impregnated wire.

Finally, acceptable results were obtained with water jet cutting. The notches and the circular holes, needed for loading, were produced at a local shop. Clean slits were possible but the thinnest achievable gage was 0.040". *A priori*, diamond coated wire would be capable of improving on that but it was not possible to find a commercial shop that would do that kind of work. With the aid of a simple scroll saw and some commercially available diamond impregnated steel wire, we were able to extend the notches to the geometry shown in Fig. 12. Longer extensions were impossible because the wire would snap or a non-straight cut would result. For further work, thin slits could be achieved with more precise tools and feeding mechanisms.

The Loading Fixture

To provide stable crack propagation, an arrangement of displacement controlled loading was considered in order. The special circumstances of the experimental setup and techniques to be used basically drove the design of the loading fixture; a photograph and a schematic are shown in Fig. 13. In the image, the fixture carries one of the large specimens and is mounted in an Instron testing machine. The loading fixture was designed and fabricated at our facility.

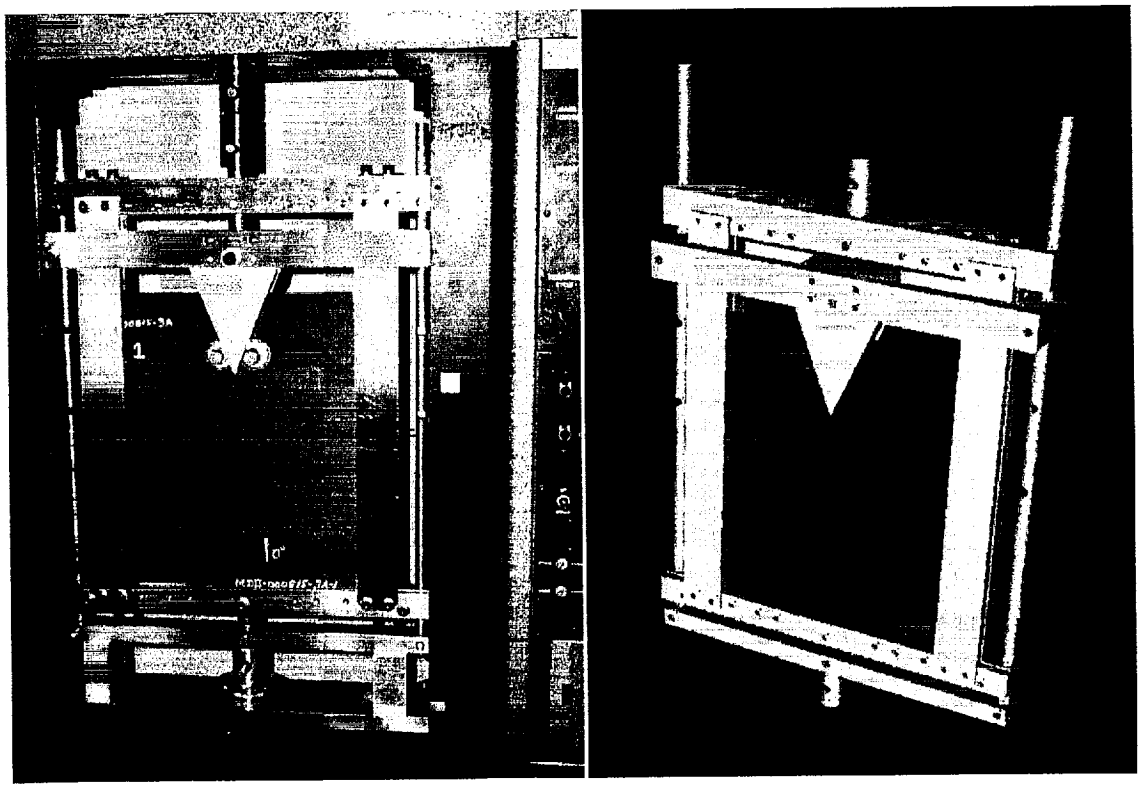

Figure 13. Loading fixture. Diagram and photograph with a large specimen mounted in an Instron testing machine.

The fixture was designed in this manner so that the crack is opened under displacement control via a wedge and pins on needle-roller bearings. Second, the specimen is supported along its edges to stabilize it against buckling or out of plane

displacement. Previous Finite Element Analysis calculations highlighted the occurrence of buckling, especially for the larger panels, as is shown in Fig. 14.

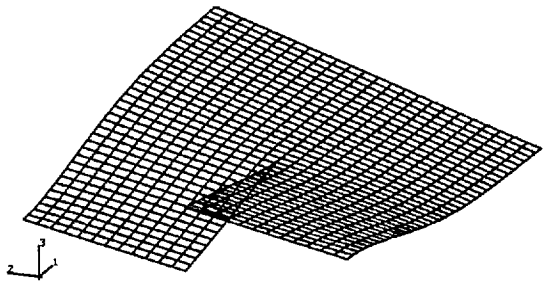

Figure 14. Finite Element simulation of Mode I crack loading indicated that the specimens would be prone to buckling and out of plane displacements.

In the experimental set-up crack is oriented along the vertical direction to facilitate the introduction, penetration and symmetric retention of x-ray-opaque media – Tetrabromoethane (TBE) or Diiodomethane (DIM)—into the crack front region. These compounds allow the identification of delamination and internal damage through x-ray imaging, as has already been explained before.

The specimen must remain fixed in space during the tests, i.e., rigid body motions and rotations need to be prevented or minimized to facilitate the Digital Image Correlation (DIC) process. Otherwise, errors would have been introduced in the measurements and, also, it would have been very difficult to position the CCD camera so as to follow the displacements. This presented a challenge since typically all the testing machines (Instron, MTS) are fixed on the top and provide loading from the bottom. This would have suggested to drive the wedge from the bottom up into the crack but, as previously mentioned, this idea was discarded because of the need to use

gravity to have the penetrants for PEXR introduced and retained. Therefore, the wedge had to be driven from below but down and the solution chosen was to use the side bars that are connected to the wedge assembly by means of shear pins.

The anticipated loads for these tests would also be very high (circa 60,000 lb) and another constraint was the space available in the frame of the Instron or MTS testing machines. This made necessary the use of high strength steels for some parts of the loading fixture, e.g. the side bars were made of precipitation hardened 17-4 stainless steel because of their small diameter and the stress concentration provoked by the shear pin holes. Other alloys were considered, for example 4140 and 4340 heat treated steel, but the particular dimensions –long, narrow, straight bars—of these parts would prove very difficult to be manufactured in that way because the heat treatment would introduce residual stresses that would bend the bars and would leave them too brittle. These problems were avoided with the material selected.

Finally, it was very desirable to be able to use only one loading fixture for specimens of different sizes to explore the influence of this variable in the damage process.

Originally, the wedge had an angle of 44° but was later redesigned to be shallower (20°) to reduce the component of compression as the loads increase for the larger specimens. All small specimens were tested using the 44°-angle wedge.

Other modifications that became necessary as larger panels were tested were related to the loading pins, i.e., the pins against which the wedge runs. This fact called for heat treatment to harden the surface but that made the pins brittle and, as the loads increased, some of them failed. Thus larger diameter pins were used to better distribute the loads and also to have a thicker cross-section to increase rigidity and better accommodate the bending moments. The original loading pins had a ¾" diameter whereas the latest design 2.16".

Test results and current status

All small size specimens (6 × 6 in) have been successfully tested to failure and a detailed "history" of the damage progression—both in the interior and the exterior of the material—have been recorded through x-ray radiographies and DIC calculations. Figure 15 very well exemplifies this.

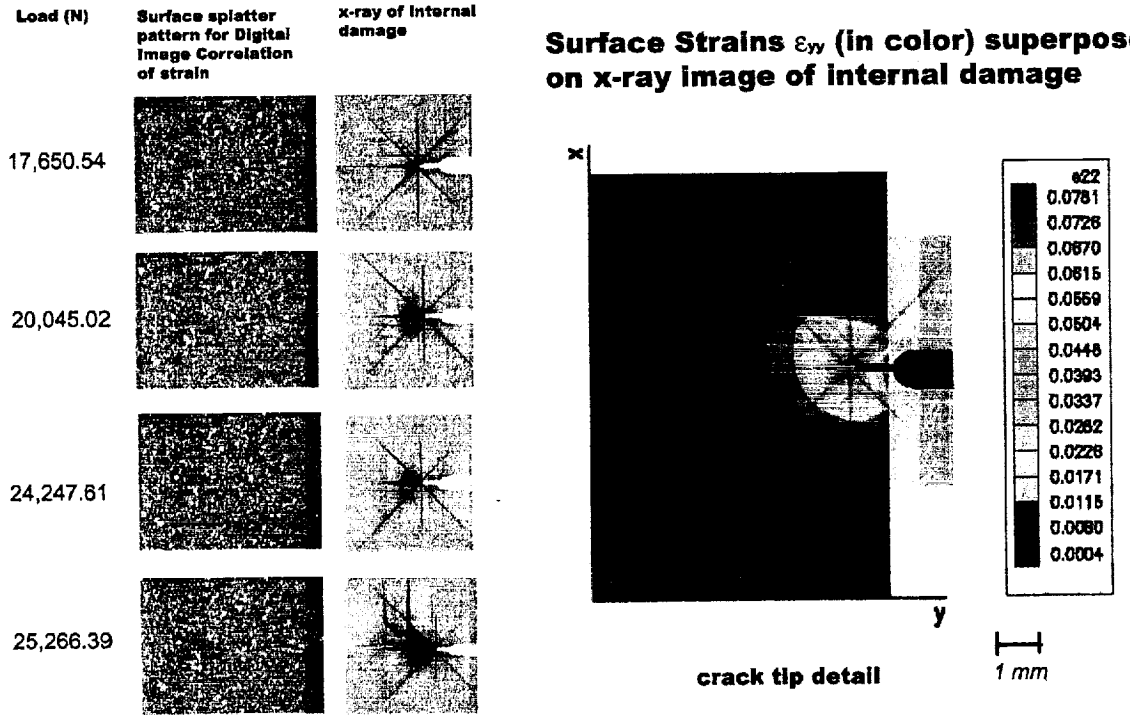

Figure 15. Damage progression under load at the crack tip and superposition of the information provided by x-rays and digital image correlation.

Preliminary analyses of the results suggest that failure starts and propagates at the interface between the fibers and the matrix. Even the delaminations would occur along this path. The x-ray images and some SEM photographs (Fig. 16) seem to support this claim.

Figure 16. The main failure mechanisms in our tests are the interface fracture between fibers and matrix and fiber breakage.

Although the analysis of the data is at an early stage, some observations can be made:

1) The lay-up does not appear to have a great influence on the load of crack initiation;
2) the samples with the outer layers at 90° with respect to the crack loose the outer layer (in narrow bands) through delamination and buckling of the whole layer (Fig. 17)

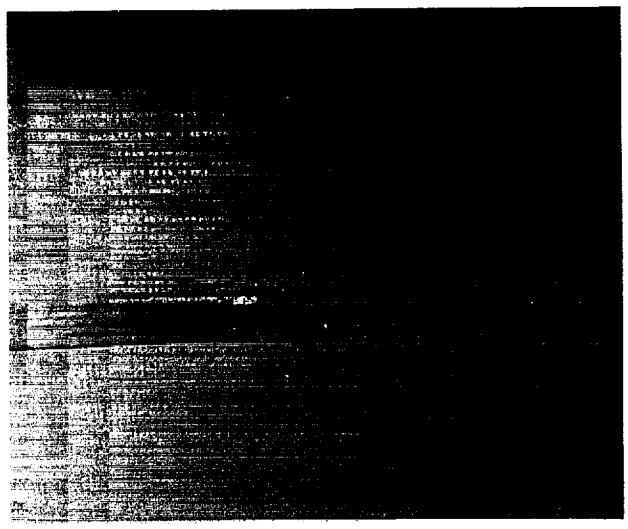

Figure 17. After loaded up to 5000 lb, damage is present at the surface in the form of delamination of a sliver along the fiber direction and fiber breakage.

The DIC calculations also allow us to appreciate the geometrical characteristics of the strain field around the crack tip. In figure n. these are presented superimposed on a vector plot of the deformations.

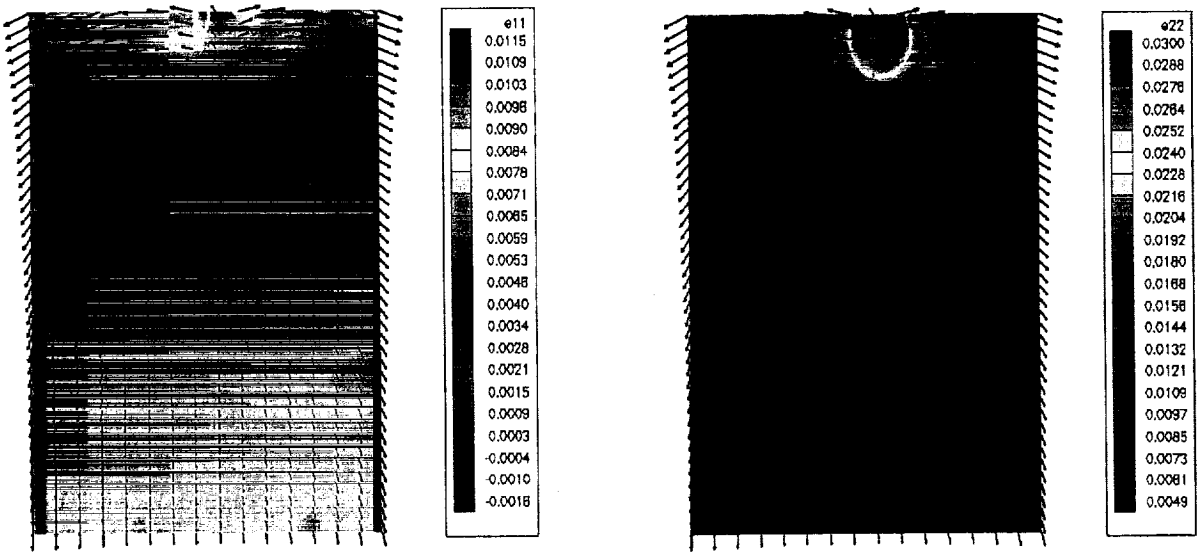

Figure 18. Displacement and strain (ε_{11}, ε_{22}) fields calculated by means of the digital image correlation technique for the region shown in fig. 5. The graph on the left is a plot of ε_{11}, i.e. the strain parallel to the crack (vertical direction in this illustration) while that on the right shows ε_{22} or the strain perpendicular to the crack direction.

After the tests on the small panels were completed, those on the medium sized samples (12 × 12 in) were started. At that time the experiments had to be stopped since the necessary loads were higher than anticipated and some redesign of the loading fixture is needed. Many of the modifications have already been mentioned in the section dealing with the design of the loading fixture.

Phase II

The following section reports the results of the prior project executed under the grant. As mentioned before, we choose to report this through the inclusion of published papers on the topic.

Applied Composite Materials **5:** 273–287, 1998.

Failure of Laminated Composites at Thickness Discontinuities – an Experimental and Analytical Study

SANGWOOK LEE* and WOLFGANG G. KNAUSS**
Graduate Aeronautical Laboratories, California Institute of Technology, Pasadena, CA 91125, U.S.A.

(Received 20 January 1998; accepted 2 March 1998)

Abstract. Failure initiation of laminated composites at a thickness discontinuity is studied experimentally with the aid of an optical microscope under combined loading of tension, transverse shear and bending, making use of three- and four-point bending arrangements. Because transverse shear produced relatively small effects in failure initiation, results are presented as tension-bending interactions. Two loading frames for three- and four-point bending were designed to apply moment and tension simultaneously to produce failure by generating a ply crack; this initiation was evaluated by finite element analysis using ABAQUS. For cross-plies bounding the interface at the base of the step it is found that a maximum strain criterion applied to the continuing (long) ply describes the failure initiation. Ultimate failure resulted at loads on the order of 25 to 35% higher than those at failure initiation.

Key words: composite, failure, failure initiation, thickness discontinuity, combined loading.

1. Introduction

Structures typically are subject to stress concentrations and/or singularities which are caused by a variety of geometries such as cutouts or openings, sudden changes in thickness, joints (bolted, bonded), mismatch of elastic properties between two adjacent components, and voids due to material fabrication. However, in spite of the importance of stress concentrations to failure initiation, many issues related to this topic for laminated composites are still in the early stages of development [1].

Sudden thickness changes are very common in composite structures, as, for example, in stiffener-reinforced thin skins, lap joints, ply drop-off in tailored structures (helicopter rotor blades and wing trailing edges), as well as solid-sandwich transition. Because highly localized stresses are typically considered to be sources of failure, most of the earlier research focused on the determination of stresses near 'sharp' corners. Lin and Hartman [2] obtained stress singularities for bonded anisotropic wedges under generalized plane strain conditions in terms of Lekhnit-

* Graduate student.
** Professor of Aeronautics and Applied Mechanics.

skii's complex variable method (complex eigenvalue problem). Zenkert et al. [3] applied this result to suggest a failure criterion for fracture initiation at sharp 90° corners in an imperfect butt joint by assuming that onset of fracture may be predicted in terms of a (corner) stress intensity factors and a fracture toughness parameter. Kassapoglou and DiNicola [4] suggested an efficient stress estimate at skin-stiffener interfaces to reduce the cost of theoretical and finite element analyses, the results being intended for use by structural designers at the early stages when trade-off studies are performed. For the same purpose Bhat and Lagace [5] presented an estimation method for a quick evaluation of interlaminar stresses at material discontinuities. Experimental studies on the effect of ply-drop configuration on delamination strength have been carried out by Botting et al. [6] with an attendant (three-dimensional) finite element analysis to determine maximum shear and von Mises stresses as a measure of delamination initiation. In a similar vein Hyer et al. [7] determined stresses experimentally around a stiffener/skin interface in pressure-loaded composite panels to reveal the three dimensional nature of stresses around sharp corners. These studies essentially focused all on the effects of very localized (small size scale) singularities or stress concentrations.

As part of the motivation for the work reported here, Kubr [8] performed numerical studies in our own laboratories and showed that the spatial extent of the singularity is scaled by the ply-thickness and thus extremely small. The stresses were found to be of the form $\sigma_{ij} = \Psi_{ij} r^k$ and thus similar to the Williams solution at a wedge in an isotropic material [9]. Employing a highly refined finite element mesh, plots of $\log(\sigma) - \log(r)$ were used for each stress components to determine k and Ψ by fitting a straight line to the log-log plots, the procedure followed also by Zenkert *et al.* [3]. However, it turned out that the power law stress singularity field applied only within a region of less than 10^{-1} μm from the base of the corner, the solution deviating markedly from the assumed power law outside of that domain. Considering that the fiber diameter is about 5 μm, the singularity field exists thus in such an extremely small region that continuum concepts for 'smeared-out' ply properties are not applicable at that size scale.

In an experimental follow-on study Gortsema [10] showed with the aid of optical microscopy that in a realistic situation, i.e. in the absence of a 'mathematically sharp corner'*, the location of a stress singularity was not the immediate site of failure initiation. Failure originated consistently at points away from the interior corner of the step-down; this distance from the 'corner' was measured typically in terms of one or a few ply-thicknesses. The Kubr–Gortsema studies thus demonstrated clearly that failure initiation from a corner is not optimally formulated in terms of singular stress fields.

As a consequence of these findings the following study concentrates on exploring the failure near thickness variations in terms of more conventional structural rather than continuum mechanical terms, though the analysis detail may have to

* Microscopic examination of 'corners' reveals quickly that even in carefully prepared specimens, typically a (rough) fillet exists, the radius of which is on the order of a ply-thickness.

be carried out at the sub-ply-level as the finest material resolution. Moreover, it is of interest to explore the characterization of failure (initiation) in terms of load parameters that are typically used in structural (design) analysis, rather than in terms of micromechanics concepts addressing the problem scale governed by fiber diameters or smaller. Accordingly we present here the experimental arrangement and attendant finite element analysis necessary to establish criteria for failure initiation near thickness variations. Along with that presentation we cite results for a particular lay-up across the step geometry, being fully aware that different lay-ups result in different failure behavior. Further studies along this line of investigation are presented in a separate paper [11].

In the sequel we present first, in Section 2, the experimental equipment and measurement methods and in Section 3 selected results of failure appearance at the microscope level. In Section 4 the analysis based on the commercial finite element code ABAQUS is presented along with an example analysis of the failure illustrated in Section 3. The paper concludes with a section summarizing the observations and possible variations of the observed behavior as a function of different ply lay-ups.

2. The Experimental Set-Up

The experimental work comprises three major components, namely the design and manufacture of the specimens, the means of providing the combined loading and the method of observing failure initiation. We consider these items sequentially next.

2.1. SPECIMENS

The geometry of a typical specimen used in this study is shown in Figure 1. Because structures contain, in general, multidirectional plies, a finite width specimen develops, per force, three-dimensional deformations in the vicinity of the corner, and, in fact, all along the edges of the specimen [12]. There was no simple, economical way to obviate this disadvantage in favor of a more two dimensional configuration; this fact has both experimental as well as analytical consequences that need to be address without approximation.

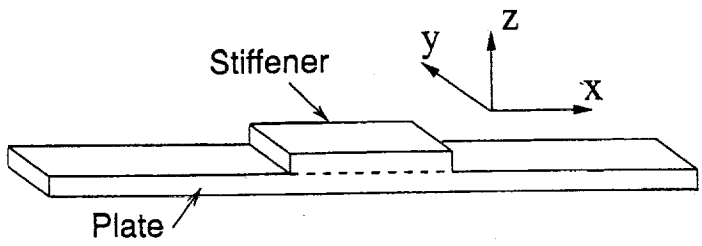

Figure 1. Specimen configuration.

The specimens were manufactured of AS4/3502 carbon fiber reinforced epoxy at the NASA Langley research center. The thicker portion of the specimen (stiffener) was co-cured with the base plate. The specimens were fabricated as a single, stepped plate, which was then cut with a diamond blade into individual specimen strips. After the specimens were cut, each one was C-scanned to ensure that neither delaminations nor inclusions could be observed*. The cut edges of the specimens were polished with a 3000 (6 μm) grit diamond paste in order to reveal the fiber structure and to allow succinct observations of failure initiation. The present study addresses the lay-up of the substrate of the plate as $[90, +450, -45]_s$ and $[0, -45, 90, +45]_s$ for the stiffener; the interface is formed by a 90° ply in the plate and a 0° ply in the stiffener, with 0-directions running parallel to the x-axis as shown in Figure 1, and positive angles measure counter-clockwise from this axis.

Because of the lay-up a coupling exists between bending and twisting ($D_{16} \neq 0$), although most coupling terms vanish ($B_{ij} = 0$ for $i, j = 1, 2, 6$ and $A_{16} = A_{26} = 0$). In the experiments the twist mode was restrained in order to represent, in part, wide panels in structures as far as possible; however, the analytical model accounts for this effect.

2.2. LOADING DEVICES

In order to apply combined loading to the specimens two devices were designed as described below. However, before these details are considered it should be pointed out that tests involving three and four point bending involve different degrees of transverse shear. Because no significant differences were observed in performing three- and four-point bending, it was concluded that transverse shear played a secondary role in the failure behavior, and in the sequel only tension-bending interactions will thus be discussed.

Contrary to a test of uniformly cross-sectioned specimens simple tension applied to the ends of a specimen produces bending. The deflection and moment distribution can be estimated from beam theory. The deflection and moment distribution (with respect to the midplane) under a tension of $T = 3736$ N (840 lbs) are shown in Figure 2. Since the reference plane is different for the plate and thicker portion, a jump occurs in the moment distribution at the step-down section ($x = 4.5$ in.). The results from beam analysis are compared with those from the finite element analysis (ABAQUS) in the figure.

The straining device shown in Figure 3 was used for tests involving three- and four-point bending. It was designed to draw on the tension/torsion capability of a MTS system. The tension is provided by the test machine in the standard fashion, but the torsional mode was translated through an appropriate linkage system into a lateral force F for providing the lateral deflection. The accompanying lateral force was recorded by a compression load cell.

* We are indebted to Dr. J. H. Starnes and Mr. Allen Waters of NASA/Langley for providing the samples including cutting and C-scanning.

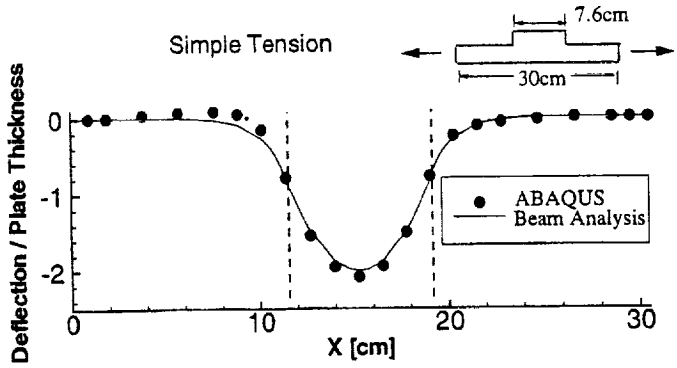

(a) Deflection

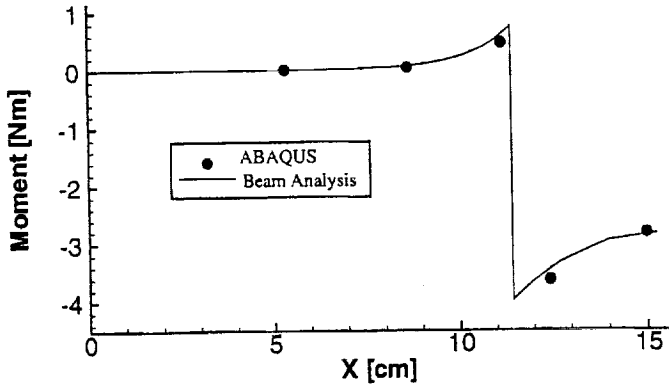

(b) Moment distribution

Figure 2. Deflection and moment under tension.

This loading device allows independent histories of deformation in the two (three) loading modes. Loading with this appliance was conducted typically by straining the specimen to a desired tensile load and keeping that load constant under load control mode. Then the lateral force was applied to bend the specimen.

A second loading frame, also used for combined tension/bending tests but under a proportional loading scenario, is shown in Figure 4. The specimen is located off the tension axis. As the specimen is pulled, both tension and moment on the step-down section increase simultaneously and roughly proportionately as shown in the loading path in Figure 4. The load path is changed by adjusting the eccentricity e. Simple tension results with this frame for some fixed value of e. As explained above, a positive bending moment exists if only a tensile load is applied. However, if e takes on some negative value, pure tension, i.e. a condition of nearly zero moment, can be achieved. The range of e was from -0.1 in. to 0.5 in. The operation

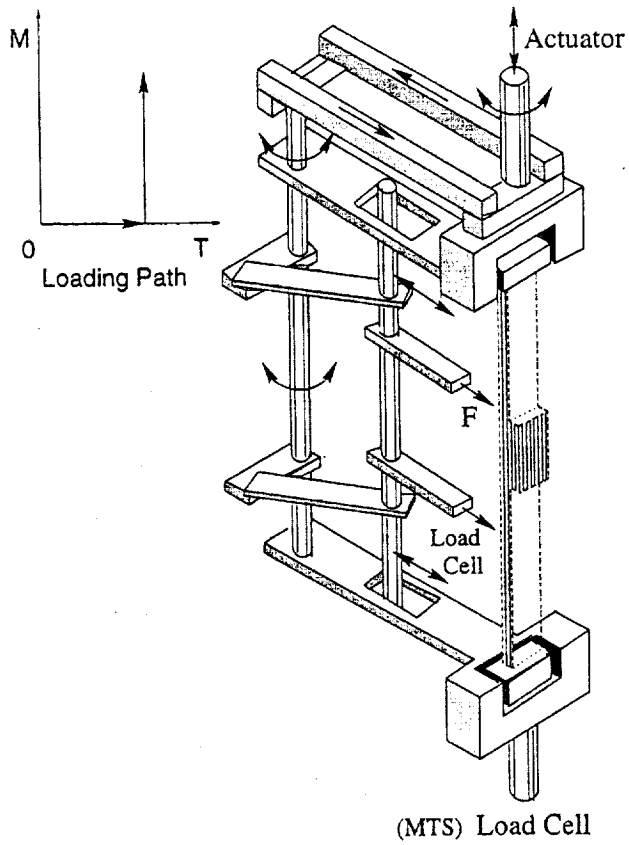

Figure 3. Loading frame for three- and four-point bending coupled with tension.

of this 'proportional loading frame' was much simpler than the other one, and was used primarily.

The bending moment M was determined by measuring the distance, w, between the line of tension and the mid plane of the step section in the deformed configuration as $M = Pw$ for a tensile load P. From this relation, it can be readily appreciated that a small error in e induces a corresponding moment error. It was thus imperative to measure w precisely.

Accordingly, the traversing device carrying a low power microscope (magnification 4×) in Figure 5 was used. The resolution of the device was 0.001 in. This method was also selected to measure w because its non-contact method of operation can also be used for measurements at elevated temperatures. Any type of contact measurement, for example a traveling indicator, can exert an undesirable lateral force on the specimen.

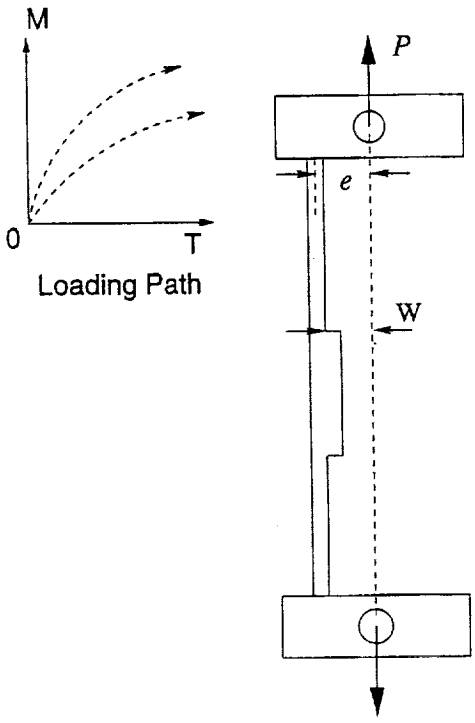

Figure 4. Loading frame for proportional moment/tension loads.

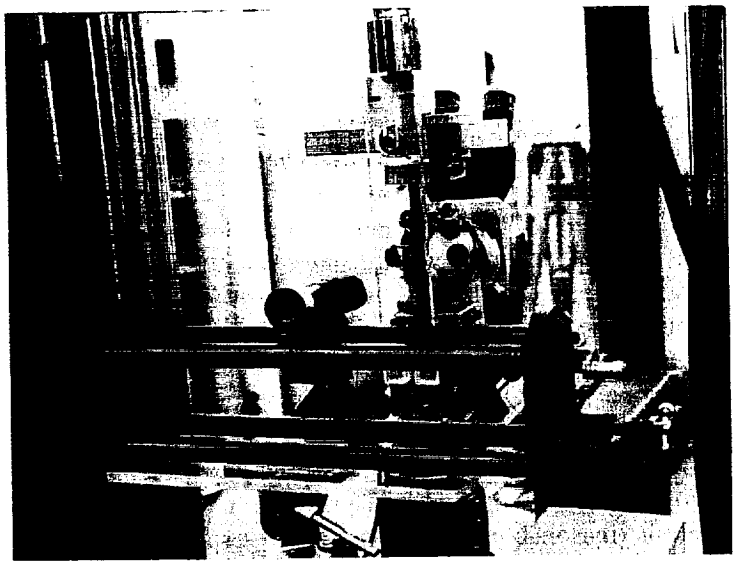

Figure 5. Traveling microscope for measuring lateral deflection.

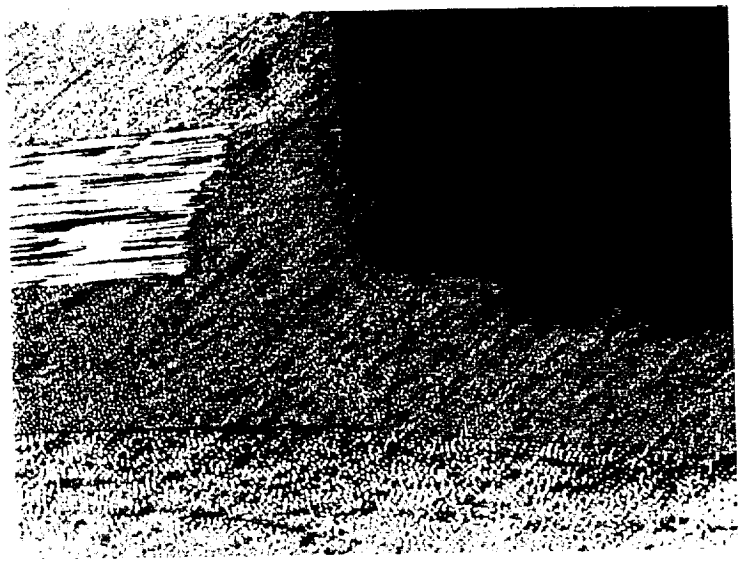

Figure 6. An example of a matrix crack in the specimen under simple tension.

3. Failure Determination

In situ observation of the free edge (surface) with the aid of a stereo microscope allowed detection of failure initiation in the form of the appearance of small cracks while the specimen was being loaded. The microscope was placed on a mount possessing three degrees of freedom. This feature provided the ability to track the corner of interest and its surroundings as its position and orientation changed during the loading process. Attachment of photographic equipment to the microscope and the polished surface finish allowed the recording of various features in the damage development in real time during the test.

The dominant and consistent failure mode of this lay-up was by matrix cracking. In the top ply of the base of the plate specimen which is next to the interface, the fiber direction is at an angle of 90° with respect to the tension axis. The lamina across the interface has a fiber direction of 0°. Because the plies are weakest in the direction normal to the fibers, the tension/bending induced stress component normal to fibers causes the ply to crack. A photograph of a typical crack near a corner is shown in Figure 6. Some cracks occur at locations away from the corner as reported by Gortsema [10]. One reason for this behavior is the shape of the corner which is 'round' rather than sharp.

The combined failure loads initiating failure are plotted in Figure 7 along with numerical results to be described in the next section. The trade-off relation between tension and moment is (reasonably) linear. The failure responses of other lay-ups are discussed in more detail elsewhere [11].

While the emphasis in this work was on the initiation of failure as a conservative failure criterion for structural purposes, in some of the four-point bending tests,

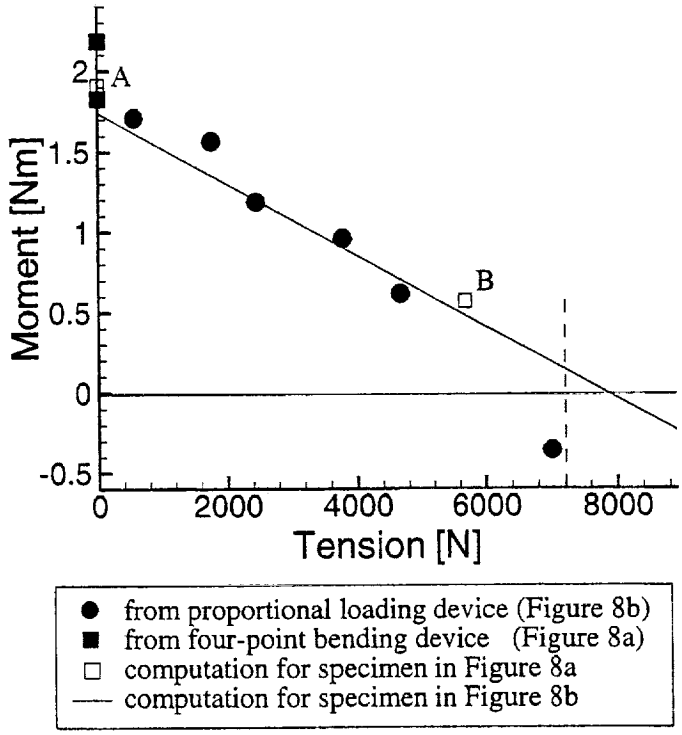

Figure 7. Failure loads from experiment and computation.

loads were increased after an initial crack appeared to check the residual load carrying capability. It was found that for the ply lay-up studied here this load at ultimate failure was about 25–35% higher than that at initiation. For further details on the crack propagation to ultimate failure the interested reader is encouraged to consult Gortsema [10]. Suffice it here to state that after the top ply had been broken in the initial fracture process, a matrix crack propagated along the interface of the first and second plies of the specimen. This (intermediate) delamination process was rather slow and virtually no sound of the process was audible. However, the next and final phase of the failure process involved further complex delaminations accompanied by noisy matrix cracking in adjacent plies.

4. Finite Element Analysis

A rationale for the failure behavior described above was developed by means of a finite element analysis. It was clear from the detailed physical observations that the corners of the specimens, though carefully prepared for this study, were not very sharp*, and that failure initiation did not occur at the radius proper (see Figure 6, as

* In terms of Kubr's analysis 'sharp' should be measured in terms of a radius of curvature that is very small compared to a lamina thickness.

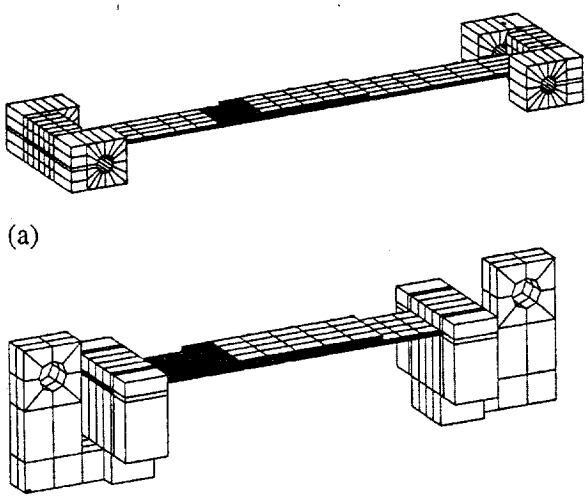

Figure 8. Coarse finite element meshes for the two loading devices: (a) Three and four point bending; (b) Mesh for proportional loading.

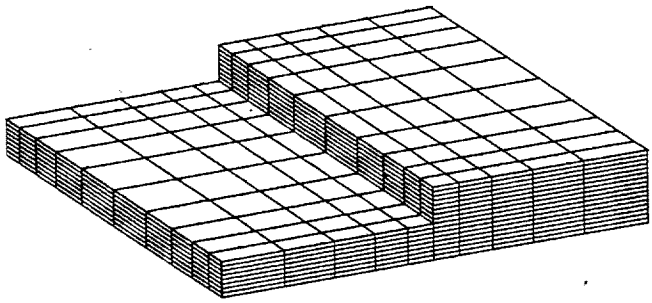

Figure 9. Submodel.

well as the discussion in Section 3). Accordingly it was not deemed necessary to address this problem with a singularity in mind and that the element mesh did not need to be extremely small in the neighborhood of the corner. Specimens as loaded by the two frames were modeled as shown in Figure 8. The size of the problem (degrees of freedom) was limited through the use of incompatible elements and nonlinear analysis. For reasonable results around the corners the shaded part of the two meshes was refined further and solved by using the submodeling technique.

The submodel is shown in Figure 9. Stress (or strain) components of the submodel were computed at the integration points of the elements with the aid of the commercial finite element analysis program ABAQUS. The C3D8I element used is a three-dimensional linear brick solid elements with incompatible modes and has 8 integration points. Because of the 13 internal degrees of freedom the elements are somewhat more 'expensive' than regular displacement elements. But the elements have incompatible modes to improve the result for the bending behavior [13].

The plies were assumed to be transversely isotropic material. Each of the plies is represented in the model by one element in the thickness direction. Because the deformations are large relative to the specimen thickness, kinematically nonlinear analysis is employed consistently.

AN EXAMPLE OF FAILURE PREDICTION: The typical strain distribution* is shown in Figure 10, where the strain components are given in directions relative to the fiber orientation. Axis 1 is in the fiber direction, axis 2 is in fiber-normal, and axis 3 is in the thickness direction. The figures show the existence of a boundary layer [12] near the two free edges, $y = 0$ and $y = 1$. Note that in conforming with typical strength of materials concepts ε_{13}, ε_{23}, and ε_{33} almost vanish except near the free edge and along the corner.

Since for the lay-up considered here the failure is in the form of matrix cracking, this suggests that a strain or stress in the fiber-normal direction is the driver of failure. The numerical results evaluated for loads equal to those at failure initiation in the experiments, showed that the maximum lamina strain ε_{22} was close to the ultimate strain ε_{ult} of a single ply ($\varepsilon_{ult} = 0.005$). Thus loading conditions were changed computationally to determine those combinations of tension and moment for which the maximum ε_{22} was equal to the ultimate strain ε_{ult}. In Figure 11, the maximum strain ε_{22} is 0.005 for four different loadings. Note that the profile of the ε_{22} distribution is nearly the same for all loading combinations. We also note that the normal strains ε_{11} and ε_{22} achieve (small relative) maxima on the edge of the specimen, as depicted in Figure 10(a) and (b), which are not symmetric with respect to the specimen centerline (parallel to the tension axis). This small difference is sufficient to cause failure initiation consistently on one side of the specimen and at one specific corner (the specimen is rotationally symmetric); this fact made it possible to locally and systematically observe the failure initiation with a microscope.

The numerically determined failure load interactions are compared with experimental results in Figure 7. In spite of the (kinematically) nonlinear behavior of the specimen the relation between the moment and the tension at failure is linear, as conjectured in Section 3. Moreover, the figure demonstrates rather good agreement of the computations with the experimental results, indicating that a maximum lamina strain criterion can be used to estimate failure loads.

In this context the question arises what the appropriate (minimal) size of the finite element near the corner is to be, because for a 'mathematically sharp' corner a continued reduction in the element size results in increasing locally computed stresses. This problem can, in principle, be circumvented by modeling the true curvature of the corner configuration and making the elements small with respect to the fillet radius. This approach, while correct for the particular specimen under consideration, does not address the generic problem of how to use computations

* The location of the points represented here are at integration points about 20% of the lamina thickness below the top surface of the plate.

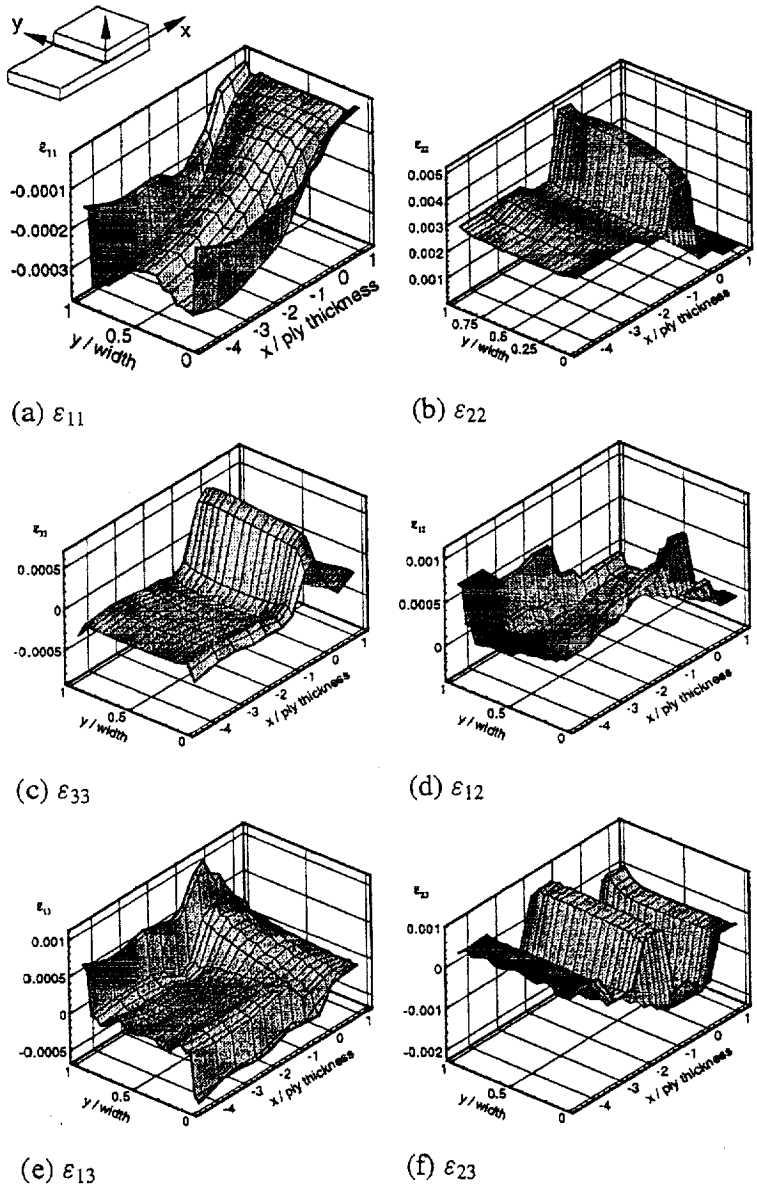

(a) ε_{11} (b) ε_{22}

(c) ε_{33} (d) ε_{12}

(e) ε_{13} (f) ε_{23}

Figure 10. Strain distribution for $T = 520$ N (117 lbs), $M = 1.6$ Nm (14.1 in.lb).

for thickness discontinuities in design related issues. An alternate method is to size the elements in a manner that is typical for the problem at hand so that the analysis renders results that are consistently in line with the experiments. Accordingly we chose to compute strains at integration points, with the distance of the integration point, where the maximum strain was computed, being about 4 times the ply thickness from the corner. This process introduces implicitly a (limiting)

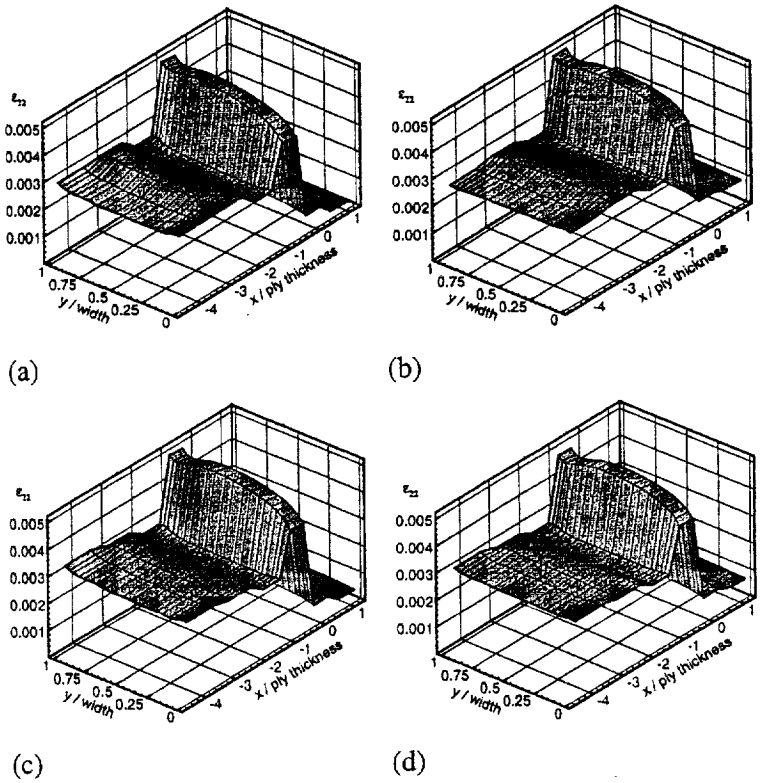

Figure 11. Strain ε_{22} under different loading: (a) $T = 520\,\text{N}$ (117 lbs), $M = 1.59\,\text{Nm}$ (14.1 in.lb); (b) $T = 5181\,\text{N}$ (1165 lbs), $M = 0.63\,\text{Nm}$ (5.6 in.lb); (c) $T = 1761\,\text{N}$ (396 lbs), $M = 1.38\,\text{Nm}$ (12.2 in.lb); (d) $T = 3825\,\text{N}$ (860 lbs), $M = 0.89\,\text{Nm}$ (7.9 in.lb).

characteristic length into the analysis, which has been advocated repeatedly before in the failure analysis of laminated composites containing (potential) singularities or stress concentrations [6, 14].

Two computation models are presented in Figure 8, both employing the same ultimate ply strain. Because of the large deformations and the fact that coupling between tension, bending and torsion could not be completely eliminated in the tests, there exists a dependence of the load level on the length of the specimen. The square symbols in Figure 7 are derived from the long specimens tested in the MTS-driven device (cf. Figure 8(a)) and the round ones from the short specimen tested in the combined loading frame (Figure (8b)). Accordingly, computations were performed to conform to these situations. In Figure 7 the straight line represents conditions derived for the 'shorter' specimens (Figure 8(b)). Computations for the longer specimens required slightly larger load levels and yielded the open square symbols designated as points A and B. The finite element analysis supports thus the experimental findings.

5. Conclusion

The failure of laminated composites at corners has been studied with special loading frames in combined bending-tension tests. For the lamination sequence studied in this paper the matrix and/or interface with the fibers in the top ply near the step-down corner failed at a constant strain across the fiber direction of 0.005% for all combinations of tension and moment applied. In addition, the strain criterion renders also the magnitude of the interaction curve in agreement with experiments. In spite of the kinematically large deformations governing the measurements, the interaction between tension and moment to produce failure initiation is linear. A finite element analysis agreed well with these experimental results. Final failure occurred at load levels that were about 25–35% higher than those at failure initiation, so that the latter is indeed a conservative, though accurate, estimate of structural failure.

Acknowledgments

This work was supported by the NASA Langley Research Center under NASA Grant NSG 1483. The authors would like to acknowledge the continued encouragement by Dr. Starnes and the assistance of Mr. Waters for providing the specimens. The finite element computations were conducted on the Cray 90 at the NSF Supported Supercomputing Center of the University of California at San Diego.

References

1. Tan, S. C., *Stress Concentrations in Laminated Composites*, Technomic Publishing Co., Inc., Lancaster, PA, 1994.
2. Lin, K. Y. and Hartman, H. H., 'Numerical Analysis of Stress Singularities at a Bonded Anisotropic Wedge', *Engineering Fracture Mechanics* **32**(2), 1989, 211–224.
3. Zenkert, D., Schubert, O. and Burman, M., 'Fracture Initiation in Foam-Core Sandwich Structures Due to Singular Stresses at Corners of Flawed Butt Joints', *Mechanics of Composite Materials and Structures* **4**, 1997, 1–21.
4. Kassapoglou, C. and DiNicola, A. J., 'Efficient Stress Solutions at Skin Stiffener Interfaces of Composite Stiffened Panels', *AIAA Journal* **30**(7), 1992, 1833–1839.
5. Bhat, N. V. and Lagace, P. A., 'An Analytical Method for the Evaluation of Interlaminar Stresses Due to Material Discontinuities', *J. Comp. Mater.* **28**(3), 1994, 190–210.
6. Botting, A. D., Vizzini, A. J. and Lee, S. W., 'Effect of Ply-Drop Configuration on Delamination Strength of Tapered Composite Structures', *AIAA Journal* **34**(8), 1996, 1650–1656.
7. Hyer, M. W., Loup, D. C. and Starnes Jr., J. H., 'Stiffener/Skin Interactions in Pressure-Loaded Composite Panels', *AIAA Journal* **28**(3), 1990, 532–537.
8. Kubr, T. J., 'Stresses Near a Change of Thickness in a Continuous-Fiber-Composite Plate', Aeronautical Engineer's Thesis, Graduate Aeronautical Laboratories of the California Institute of Technology, Pasadena, CA 91125, 1990.
9. Williams, M. L., 'On the Stress Distribution at the Base of a Stationary Crack', *J. Appl. Mech.* **24**, 1957, 109–114.

10. Gortsema, S. C., 'An Experimental Investigation of the Failure of a Stepped Composite Plate', Aeronautical Engineer's Thesis, Graduate Aeronautical Laboratories of the California Institute of Technology, Pasadena, CA 91125, 1992.
11. Lee, S. and Knauss, W. G., 'Failure of Laminated Composites at Thickness Discontinuities under Complex Loading and Elevated Temperatures', GALCIT-SM Report 98-1, Graduate Aeronautical Laboratories of the California Institute of Technology, Pasadena, CA 91125; submitted to *Int. J. Solids and Structures*.
12. Pipes, R. B. and Pagano, N. J., 'Interlaminar Stresses in Composite Laminates under Axial Extension', *J. Comp. Mater.* **4**, 1970, 538–548.
13. ABAQUS, *Theory Manual*, version 5.5, Hibbit, Karlsson and Sorenson, Inc., Providence, RI, 1995.
14. Whitney, J. M. and Nuismer, R. J., 'Stress Fracture Criteria for Laminated Composites Containing Stress Concentrations', *J. Comp. Mater.* **8**, 1974, 253–265.

PERGAMON

International Journal of Solids and Structures 37 (2000) 3479–3501

INTERNATIONAL JOURNAL OF SOLIDS and STRUCTURES

www.elsevier.com/locate/ijsolstr

Failure of laminated composites at thickness discontinuities under complex loading and elevated temperatures

S. Lee, W.G. Knauss*

Graduate Aeronautical Laboratories, California Institute of Technology, Pasadena CA 91125, USA

Received 26 February 1998; in revised form 20 July 1998

Abstract

Failure initiation of laminated composites with discontinuous thickness has been studied in terms of typical structural load description (tension, shear force and bending moment) rather than in terms of micromechanics considerations. Four types of specimens of different stacking sequence were examined to determine failure initiation, analyzed subsequently via a finite element analysis (ABAQUS) and divided into two groups that evoke cross-ply failure, on the one hand, and delamination type failure on the other. For uni-directional fiber orientation in the tension direction and across the interface, failure occurs through cracking and delamination. While the initiation strength for this failure mode is significantly higher than for cross-ply configurations, the residual strength after initiation increases only marginally (10%) beyond the initiation point. For cases involving cross-plies on either side of the interface, failure initiation occurs by matrix cracking. In these cases the residual load bearing capability was 25 to 35% higher than the corresponding failure initiation loads. The data are analyzed in terms of the Tsai-Hill criterion and in terms of an energy release criterion that has been discretized in a manner consistent with a non-singular treatment of the step "discontinuity". Assuming that time dependent aspects of the failure process are not dominant, elevated temperatures did not change the general results of how bending and tension loads interact, provided one accounts for stresses induced thermally in the tests; however the magnitude at which the failures occur depends on the temperature, with increasing temperature leading to decreasing load tolerance.

Keywords: Composite; Failure initiation; Thickness discontinuity; Combined loading; Thermal stress

1. Introduction

A recurring problem in designing structures with fiber reinforced composite materials is the potential

* Tel: +1-626-395-4524; fax: +1-626-304-0175;.
E-mail address: wgk@caltech.edu (W.G. Knauss).

0020-7683/00/$ - see front matter
PII: S0020-7683(99)00021-9

to raised temperatures must be considered. This is especially true for polymer matrix materials which become very temperature sensitive as their glass transition temperature is approached. It is thus important to evaluate in which temperature range below the glass transition structural penalties become severe. This temperature sensitivity manifests itself primarily in terms of increased time dependent (creep) behavior, which, even at temperatures well below the glass transition (20–30°C) may give rise to accumulated effects if repeated thermal cycles are involved. Although we recognize the importance of the time dependent behavior in the failure process of composite materials we prefer to take here a somewhat simpler point of view and consider temperature merely as a parameter which affects the failure strength of the composite potentially without a major complication in the form of time dependent (creep) response of the matrix. However, it is then still of interest to ask whether the failure mode(s) or mechanism(s) of failure initiation (and progression) is changed by elevating the temperature.

It appears self-evident that the ply sequence across the "interface" between the step-up and the base plays a significant role in the failure initiation process. For definition purposes we refer to the thicker portion in Fig. 1 as the step-up or stiffener, while the thinner portion is called the plate or skin, the two portions being separated by the "interface". From a physical point of view the "interface" is formed by co-curing and as such does not represent a manufacturing interface in the sense of a "secondary" or adhesive bond. The term is used here only for spatial identification purposes. Because the layers adjacent to this interface can control the failure behavior it was appropriate to include in this study several lay-ups that are likely to be representative of a large range of possible lay-up configurations, a number of four being deemed sufficiently indicative.

The tenor of this study is primarily experimental in nature, with, however a strong component of numerical analysis to examine an analytical basis for the observed failure behavior. It is not our primary objective to present design data, but to examine the nature of the interaction between loads defined in structural mechanics parlance and to explore to what extent these interactions can be explained in terms of known failure initiation concepts, most of which are well understood in the composites community. From a hardware design point of view it is important to know whether an interaction relation is complicated or not; for, if such a relation should turn out to be linear, even in the presence of nonlinearities induced by large deformations, then a minimum number of tests are needed for design purposes to establish engineering data in a particular application, while a more complicated relationship may entail costly testing every time such information is required.

Because the details of the experimental apparatus and the basics of the numerical analysis have been described elsewhere (Lee and Knauss, 1998), it suffices to present here only a brief account to the extent that it is necessary to understand the full presentation and implications of this study. Accordingly we summarize in the next section the specimen geometry and lay-up. The experimental arrangements are described in Section 3, including identification methods of failure initiation. Failure observations are recorded in Section 4. Although the emphasis is here on failure initiation we also track the residual strength of the specimens once failure initiation has occurred to final destruction. In Section 5, this exposition is followed by a presentation and discussion of the experimental results in terms of two

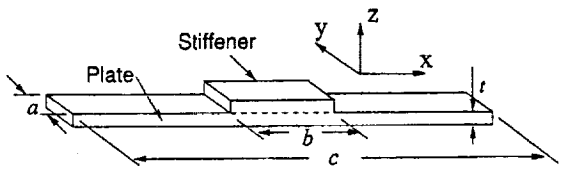

Fig. 1. Specimen configuration (c = 22.9 cm for loading device in Figure 2, c = 8.9 cm for loading device in Figure 3, b = 3.8 cm, t = 2 mm (0.08 in), a = 2.5 cm).

detail elsewhere (Lee and Knauss, 1998) and are only summarized here. One of these devices, shown in Fig. 2, employed the tension/torsion modes of an MTS testing machine to provide tension and bending by converting the twisting motion through linkages into lateral loads so as to impose bending and tension loads in arbitrary sequence (non-proportional loading). The accompanying lateral force was recorded with a compression load cell. Because of the non-uniform cross section unidirectional tension produces also bending (Lee and Knauss, 1998). Loading with this device was accomplished typically by first imposing tension, and then adding the bending. This device allowed three- as well as four-point bending. Because early test results with this apparatus evidenced no significant differences under three-*vis-à-vis* four-point bending, it was concluded that transverse shear was not of primary importance in the failure process and was, therefore, not further included in our studies.

A second device, shown in Fig. 3, provided tension and bending in proportional loading through mounting the specimen eccentrically and subjecting the grips to tension only. The range of the eccentricity "e" varied from -2.5 mm (-0.1 in.) to 13 mm (0.5 in.). By adjusting the off-set, a range of bending/tension combinations is achieved, including zero bending, to counteract the effect of the "discontinuity in the neutral axis" at the step. The operation of this appliance was much simpler than the previous one, and was used primarily. As the results derived from either loading device did not differ within the range of data scatter, the loading path was judged to be unimportant in this study.

Because the deformations were classified as "large", being on the order or larger than the specimen thickness, the bending moment needed to include the deformations. This was accomplished by measuring the distance, w, between the line of tension (centerline of the MTS grips) and the mid plane

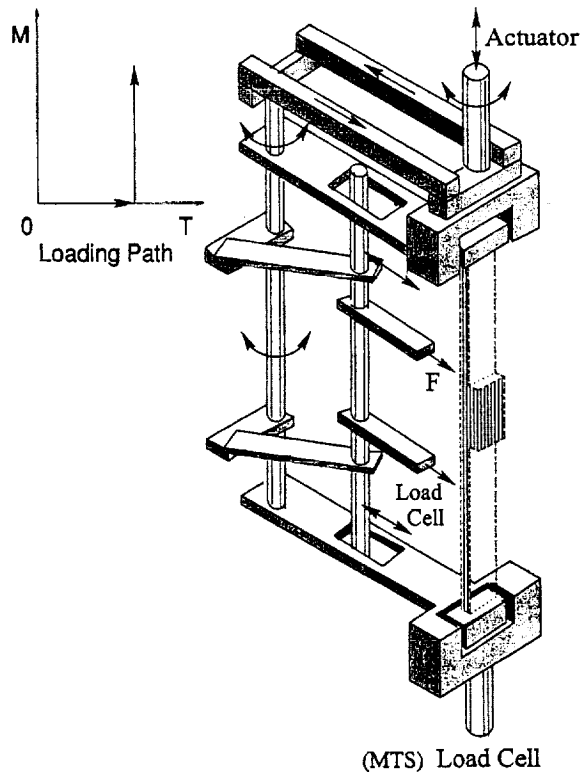

Fig. 2. Loading frame for three- and four-point bending coupled with tension.

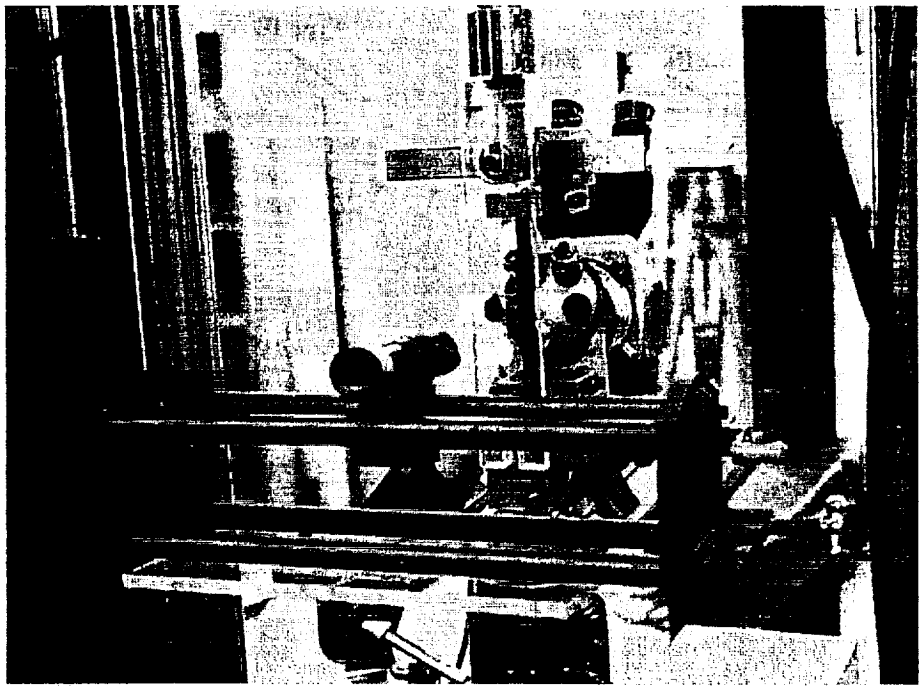

Fig. 4. Traveling microscope for measuring lateral deflection.

the other hand, the low-power observation of the deformation through the traveling microscope was still feasible.

4. Failure behavior

The failure behavior depended clearly on the stacking sequence, differentiated here primarily in terms of the ply orientation next to the interface. We delineate the major differences between these sequences and examine the commonality in their failure behavior based on accepted criteria in the fiber composites community. The experimental results are discussed first[2], followed by analytical evaluations in the next section. A summary of the failure patterns associated with the four stacking sequences is sketched in Fig. 5: Although not all laminae are shown with clarity of presentation in mind, the ply orientation near the interface is properly identified.

4.1. Type I and Type II specimens

The failure response of these specimens is governed by the similarity in the specimens: For both types the stacking sequence of the plate are the same, though the stiffeners possess different ones, namely $[0,-45,90,+45]_s$ for Type I and $[90,-45,0,+45]_s$ for Type II, so that the stiffener lamina next to the interface has either a 0° or a 90° orientation. As sketched in Fig. 5, cracking occurred in the top ply of the plate where the (maximum) tension acted across the fibers. The interaction between moment and

[2] The relative paucity of data results from a limited supply of specimens and was not a matter of convenience.

failure onset: On first hearing the characteristic noise, the test was stopped and the surface examined for cracks with the microscope and with a dye-penetrant. A picture of the latter situation is reproduced in Fig. 7, and the failure interaction data is presented in Fig. 8. Moreover, as for the previous types of specimens, complete specimen failure occurred again at about 25 to 35% higher values than those that initiated failure.

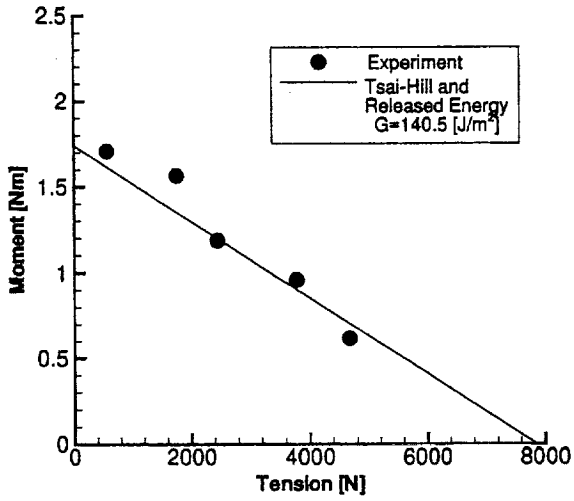

(a) Type I

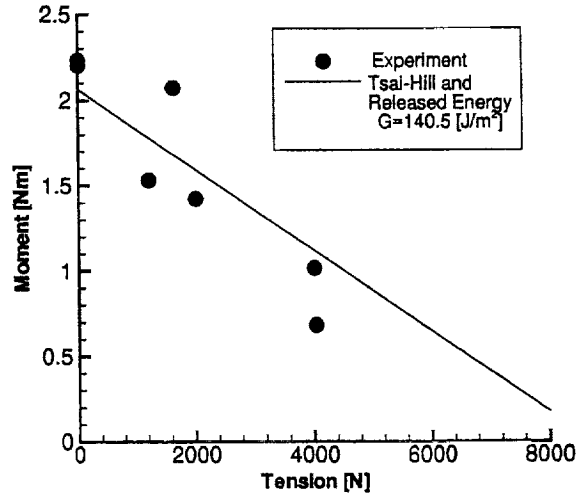

(b) Type II

Fig. 6. Moment-tension interaction for failure initiation in Type I and II specimens.

Fig. 9. Delamination initiation in a Type IV specimen.

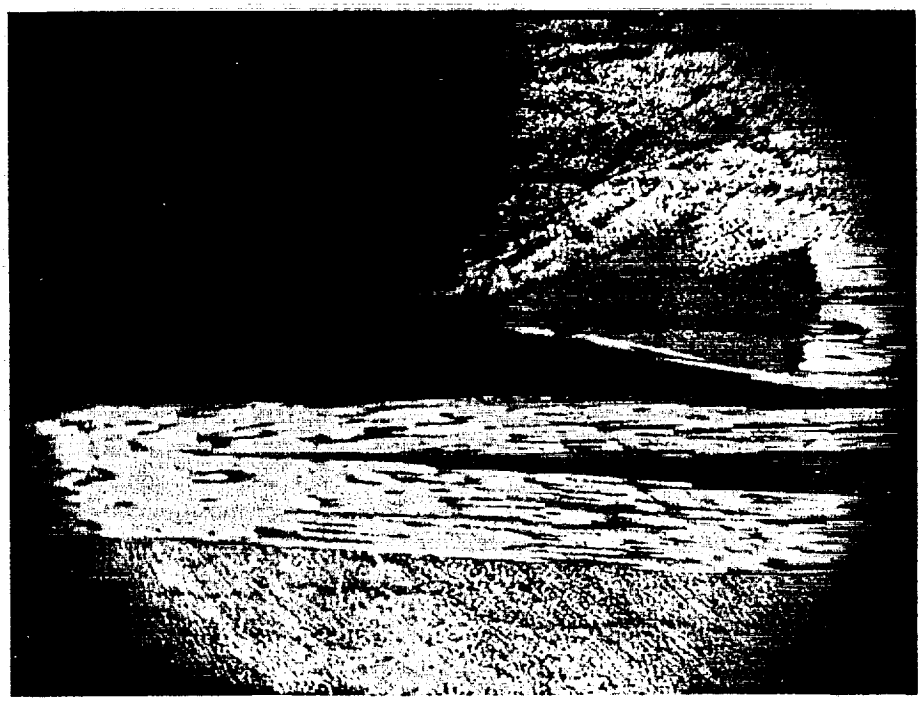

Fig. 10. Delamination and bridging in a Type IV specimen.

more detail in connection with the energy based criterion. We reserve consideration of the analytical agreement or disagreement with the experimental results until all situations have been considered.

It suffices to point out here that the analysis was fully three-dimensional, each lamina being represented by a homogeneous, anisotropic medium; use of the ABAQUS code typically involved over 13,000 degrees of freedom for the base problem on a Cray 90. As developed in Lee and Knauss (1998) a sharp corner was avoided in the analysis through choosing the element size in the corner vicinity appropriately large.

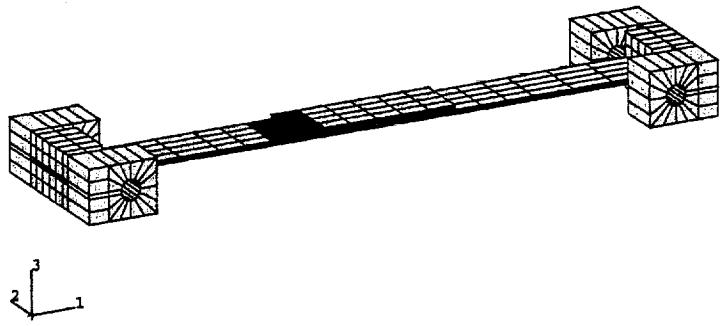

(a) Three- and four-point bending

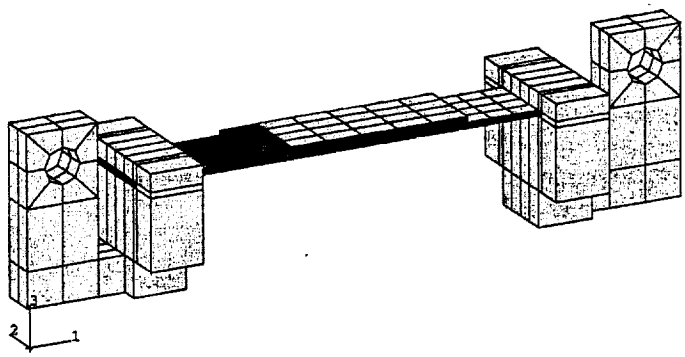

(b) Mesh for proportional loading

Fig. 12. Coarse finite element meshes for the two loading devices (the dark areas are domains for submodeling). (a) Three- and four-point bending. (b) Mesh for proportional loading..

other specimens. Accordingly, we show in Fig. 11 the curves for three values of the element size. For comparison with the results in the next section, note that these relatively small changes in the element size occasion sizable variations in the loading at failure initiation.

5.2. Energy release rate computations

The concept of the energy release rate arises typically in fracture mechanics problems where it is associated with the propagation of a pre-existing crack by an arbitrarily small (infinitesimal) growth step. In the present study the initial geometries are all considered to be crack-free, so that, strictly speaking, energy release rates are not defined. However, we apply this concept to situations where a small but finite crack length is generated from an initially (and apparently) crack free geometry, and refer to this discrete process as the (discretized) energy release rate procedure.

The method for determining the energy release rate G was similar to the finite element formulation of a crack closure integral technique employed by Rybicki et al. (1977). Essentially the same discretization is used for the crack-free geometry to evaluate the deformations and stress states in the sample along with its supports that was used for the computations involved in evaluating the Tsai–Hill criterion. Deviations from this practice will be discussed as they arise. Two submodels, one with and one without a crack (*cf.* Fig. 13) were analyzed (using the same boundary conditions) and the difference between the total strain energies of the two models was determined to represent the energy release rate G.

One question that arises again naturally concerns the length of the crack generated under these circumstances. In the case of trans-laminar fracture the crack typically appears "suddenly" across the whole thickness of the lamina. It is thus natural to accept the lamina thickness as the prevalent crack extension dimension. On the other hand, when the crack propagates parallel to laminae and parallel to the fibers as demonstrated later for specimens of the Type IV, the crack extension distance for analytical purposes is not predetermined. For this reason, a parametric study has been included that varies the crack extension distance to assess the sensitivity of the method to variations in the initiated crack length: We ask then, what energy release rate is required to make the computations agree with the measurements. Thus, subsequently determined energy values are the result of optimally fitting the analysis to the experimental data.

5.2.1. Type I and II specimens

Fig. 14 demonstrates the appearance of a crack (model) at the base of the step. The computations

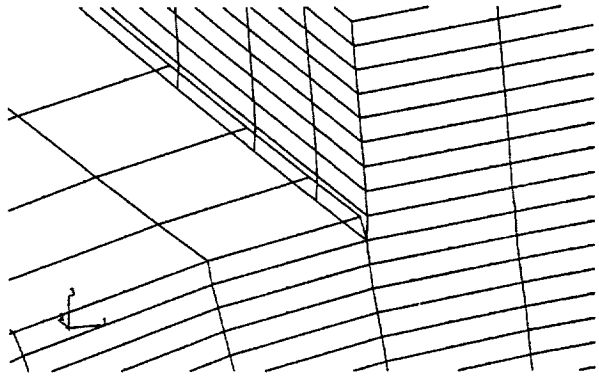

Fig. 14. Submodel detail of a crack for Type I and II specimens.

to be a function of the stacking sequence, at least at the size scale of comparison underlying the present study:

To examine whether closer agreement can be achieved (same energy values for all specimens) if the analysis is carried to the size level of the fibers was considered to be beyond the scope of the study, and needs to be investigated separately. So much seems clear, however, that the significantly higher value of the energy level for the Type IV specimens is, most likely, the result of multiple fractures at different levels through the thickness of the two adjacent zero-orientation layers; this is the same arrangement that leads to fiber bridging in a continuing intralaminar fracture or delamination process.

5.3. Discussion

Let us examine the consistency of both failure criteria to "explain" failure initiation and whether one or the other criterion provides a "better" estimate. To start with, we note that either criterion provides for an essentially linear interaction between tension and bending for Types I, II and III, but a roughly parabolic characteristic for those of Type IV. For specimen Types I–III (Fig. 6(a), Fig. 6(b), Fig. 8) only one numerical-analytical trace is shown for both the Tsai–Hill or the energy criterion: Within computational resolution there was no distinction. The other reason for this "coincidence" was that the energy release rate G was adjusted to render the same trace, but the energy criterion and the Tsai–Hill criterion provided the same slope. With respect to Fig. 11 one may argue that the energy criterion provides a somewhat better representation of the experimental data than the Tsai–Hill criterion. What makes that proposition somewhat more attractive is the fact that a single fracture energy renders this result with a relative insensitivity to the size of the finite element discretization and/or the postulated crack length. By implication this result indicates that the issue of fillet radius or finite element size scale is minimized if an energy approach is taken for a lay-up exemplified by the Type IV specimens.

Although the functional representation of the failure data by the energy criterion appears to be good, one must question this uniformity in terms of the single-valuedness of the energy release rate parameter. Type I and II specimens should involve essentially the same parameter by virtue of the fact that the lay-

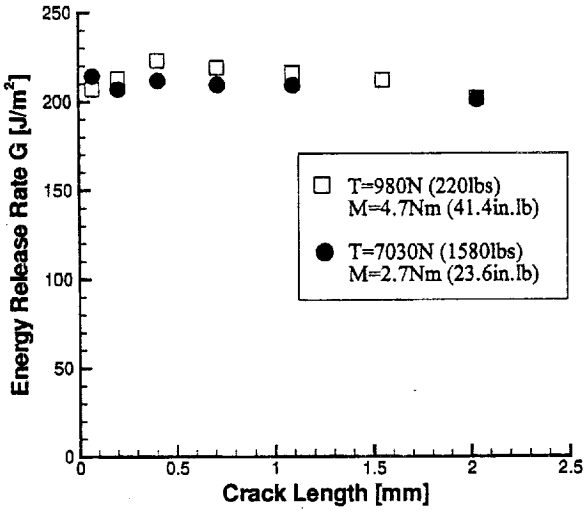

Fig. 15. Sensitivity of the discretized energy release rate to the size of the released crack surface in Type IV specimen for two loading conditions (h = 0.25 mm).

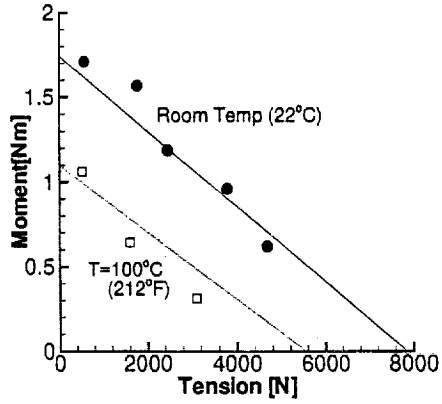

Fig. 16. Moment-tension interaction at failure initiation for Type I specimens at two temperatures.

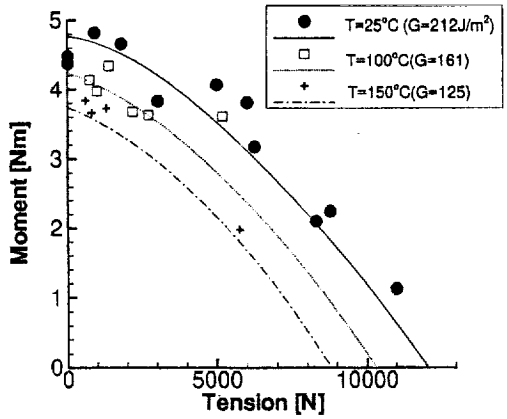

Fig. 17. Moment-tension interaction at failure initiation for Type IV specimens at three temperatures. Curves are based on energy release rate computations.

The test results and corresponding computations are delineated next. Because the modeling has been considered in some detail on the room temperature data, not all the computations were repeated for the data obtained at elevated temperatures. The specimens of Type I are analyzed in terms of the Tsai–Hill criterion only. No data could be acquired for the Type II or III specimens.

6.1.1. Type I

Testing specimens of Type I at 100°C exhibited identical failure characteristics to those at room temperature: The failure mode was again by transply matrix cracking. However, the magnitudes of the failure loads were lower than those at room temperature: Fig. 16 shows the comparison of the data with the numerical fit according to the Tsai–Hill criterion.

6.1.2. Type IV Specimens

Again, as for specimens of Type I, the failure loads at elevated temperatures for this specimen type were lower than those obtained at room temperature. However, the relative differences are now smaller

data for the separate lay-ups, we have refrained from doing so in the interest of applying a uniform criterion to all tests and configurations. Although the following observation is not perfect nor unequivocal, the delamination governed failure appears to be represented somewhat better by an energy criterion. This observation is consistent with the mode of failure progression and turns out to be rather insensitive to the size of the release increment. By contrast, the Tsai–Hill criterion requires a closer definition of an effective size scale (element size) near the step for Type IV specimens.

In the range studied, the effect of temperature on the failure manifests itself primarily in a lowering of the load levels, leaving the modes of failure unaltered. While at temperatures within a few degrees of the glass transition this behavior may change, particularly as the result of more time dependent material response, in the presently used environment higher temperatures primarily reduce the material strength. To describe a consistent failure behavior one must incorporate the thermally induced stresses in the overall evaluation, to the degree that the latter contribute a significant portion of the total and final stresses.

The specimens exhibiting the delamination mode of failure (Type IV specimens) provided the highest strength as measured by load carrying ability. They are nearly twice "as strong" as the other types of specimens which failed by ply fracture. However, the "stronger" configuration allowed for a markedly smaller (10%) difference between loads at failure initiation and final (total) failure than the ply-failure modes; the latter provided an additional load carrying capability of about 25 to 35% beyond that at failure initiation.

Acknowledgements

This work was supported by NASA Langley Research Center under NASA Grant NSG 1483. The authors would like to acknowledge the continued encouragement by Dr. J. Starnes and the assistance of Mr. Waters for providing the specimens. Substantial portions of the finite element computations were conducted on the Cray 90 at the NSF supported Supercomputing Center of the University of California at San Diego. We thank Dr. N. Pagano of the Air Force Materials Laboratory at the Wright Aeronautical Laboratories, for referring us to the data for AS4/3501-6.

Appendix A. Material information

The specimens were prepared by first forming the skin or plate from eight plies of prepreg material placed on a bleeder cloth that rested on an aluminum support plate. At this stage the pre-assembly was degassed (vacuum exposure) in the "wet" condition and a second panel with the lay-up appropriate for the stiffener was prepared, from which strips of the proper width were cut and similarly degassed, before being joined "wet" to the plate (skin). The three flat sections of this stepped assembly were covered with bleeder cloth, bagged and degassed before being placed in the autoclave. The cure profile followed essentially the recipe recommended by Hercules (Hexcel), except that 689 kPa (100 psi) were used instead of 586 kPa (85 psi). The temperature was ramped to 120°C in 60 minutes and then allowed to increase slowly to reach a steady state temperature of 135°C in two hours. After an additional 40 minutes, (time = 160 minutes) full pressure was applied and maintained continuously. From 205 to 225 minutes the temperature was raised to 177°C (350°F) and held for two hours thereafter, following which it was allowed to reach room temperature over a span of 90 minutes. After an additional two hours under these conditions the pressure was released.

The resulting panel was flat (did not curve away from the aluminum support plate), which was taken as a measure of no or very low residual stresses in the panel. The strip specimens were then cut from the

Crasto, A.S., Kim, R.Y., 1997. Hygrothermal influence on the free-edge delamination of composites under compressive loading. In: Composite Materials; Fatigue and Fracture (sixth volume), ASTM STP 1285, pp. 381–393.

Gortsema, S.C., 1992. An Experimental Investigation of the Failure of a Stepped Composite Plate. Ae.E. Thesis, Caltech, Pasadena, CA.

Hyer, M.W., Loup, D.C., Starnes Jr, J.H., 1990. Stiffener/skin interactions in pressure-loaded composite panels. AIAA Journal 28 (3), 532–537.

Kassapoglou, C., DiNicola, A.J., 1992. Efficient stress solutions at skin stiffener interfaces of composite stiffened panels. AIAA Journal 30 (7), 1833–1839.

Kubr, T.J., 1990. Stresses Near a Change of Thickness in a Continuous-Fiber-Composite Plate. Ae.E. Thesis, Caltech, Pasadena, CA.

Lee, S., Knauss, W.G., 1998. Failure of laminated composites at thickness discontinuities — an experimental and analytical study. Applied Composite Materials Journal 5 (5), 273–287.

Liechti, K.M., Chai, Y.S., 1992. Asymmetric shielding in interfacial fracture under in-plane shear. Journal of Applied Mechanics 59, 295–304.

Lin, K.Y., Hartman, H.H., 1989. Numerical analysis of stress singularities at a bonded anisotropic wedge. Engineering Fracture Mechanics 32 (2), 211–224.

Rybicki, E.F., Schmueser, D.W., Fox, J., 1977. An energy release rate approach for stable crack growth in the free-edge delamination problem. Journal of Composite Materials 11, 470–487.

U.S. Army Research Laboratory, 1994. Department of Defense Handbook MIL-HDBK-17, Polymer Matrix Composites, vol. 2, Materials Properties, Materials Sciences Co., Fort Washington, PA.

Whitney, J.M., Browning, C.E., Hoogsteden, W., 1982. A double cantilever beam test for characterizing mode I delamination of composite materials. Journal of Reinforced Plastics and Composites 1, 297–313.

Williams, M.L., 1957. On the stress distribution at the base of a stationary crack. Journal of Applied Mechanics 24, 109–114.

Zenkert, D., Schubert, O., Burman, M., 1997. Fracture initiation in foam-core sandwich structures due to singular stresses at corners of flawed butt joints. Mechanics of Composite Materials and Structures 4, 1–21.

Mechanics of Time-Dependent Materials **4:** 1–7, 2000.

A Note on the Determination of Relaxation and Creep Data from Ramp Tests

S. LEE* and W.G. KNAUSS**
Graduate Aeronautical Laboratories, California Institute of Technology, Pasadena, CA 91125, U.S.A.; E-mail: wgk@atlantis.caltech.edu

(Received 18 November 1999; accepted 21 January 2000)

Abstract. The response of (linearly) viscoelastic material is approximately the same for ramp and true step strain histories once an initial time interval of about ten times the ramp-up time has passed. Because the loss of relaxation data during that initial time can be a substantial portion of the total (logarithmically measured) time scale, a simple method is documented for exploiting data obtained from the initial ramp history via a recursion formula. Comparison of data obtained in ramp and relaxation histories are demonstrated to yield good results within the accuracy of the test method.

Key words: creep, relaxation data, viscoelasticity

1. Introduction

By way of example we start with the observation that the relaxation modulus of a linearly viscoelastic material is defined (quasi-statically) as the result of imposing a unit step-function in time for the deformation (e.g., shear, elongation or volume change). That deformation mode cannot be achieved experimentally without invoking stress waves. To deal with the complication of such waves is both experimentally as well as analytically prohibitive for routine material characterization. As a consequence one substitutes ramp histories for the step-strain test, because the long time response in a ramp history approaches that in a step history after some time. The two responses differ measurably in the early stage of loading so that this substitution is made at the expense of not recording viscoelastic response during the initial or transient portion of the ramp-strain history. Because typical experimental ramp times are on the order of a second, this recipe requires that 'valid' data be not acquired until after about 10 seconds or more have passed. This time frame is, however, often a substantial portion of the total time for which measurements can be made without encountering other problems such as long-term instrumentation stability. It is thus appropriate to consider the following simple analysis that allows evaluation of this transient time data for the determination of

* Former Graduate Student, presently at Motorola, Libertyville, Illinois, U.S.A.
** Professor of Aeronautics and Applied Mechanics.

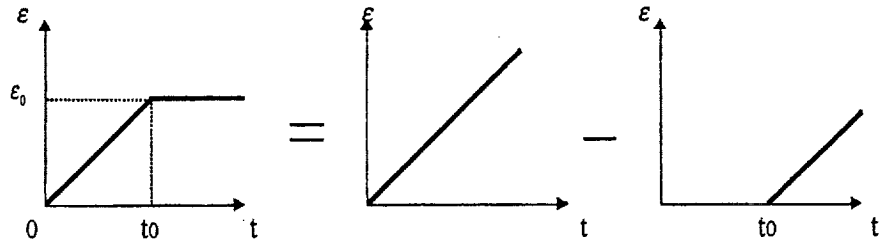

Figure 1. A ramp history of strain.

the relaxation modulus and thus increasing the range of data by typically about a decade.

2. Response in a Ramp History

Consider first the presentation in terms of shear relaxation with $\mu(t)$ denoting the relaxation modulus. As shown in Figure 1, a ramp strain input can be viewed as the superposition of two constant strain rate histories, $\varepsilon(t) = \dot{\varepsilon}_0 t h(t)$ and $\dot{\varepsilon}_0(t - t_0)h(t - t_0)$.

For a constant strain rate history $\varepsilon(t) = \dot{\varepsilon}_0 t$, the stress $\tau(t)$ is

$$\tau(t) = 2\int_0^t \mu(t-\xi)\dot{\varepsilon}\,\mathrm{d}\xi = 2\dot{\varepsilon}_0 \int_0^t \mu(t-\xi)\,\mathrm{d}\xi$$

$$= 2\dot{\varepsilon}_0 \int_0^t \mu(\eta)\,\mathrm{d}\eta = \frac{2\varepsilon(t)}{t}\int_0^t \mu(\eta)\,\mathrm{d}\eta$$

$$\equiv 2\varepsilon(t), \quad \text{where} \quad \tilde{\mu}(t) = \frac{1}{t}\int_0^t \mu(\eta)\,\mathrm{d}\eta. \tag{1}$$

Using an exemplary power law representation for the relaxation modulus

$$\mu(t) = \mu_\infty + \frac{\mu_0 - \mu_\infty}{(1 + t/\zeta_0)^n} \tag{2}$$

with μ_∞, μ_0, ζ_0 and n denoting obvious material parameters, the stress in a ramp strain history is then determined as

$$\tau(t) = 2\dot{\varepsilon}_0 m(t) \quad (t < t_0),$$

$$\tau(t) = 2\dot{\varepsilon}_0[m(t) - m(t - t_0)] \quad (t \geq t_0),$$

where

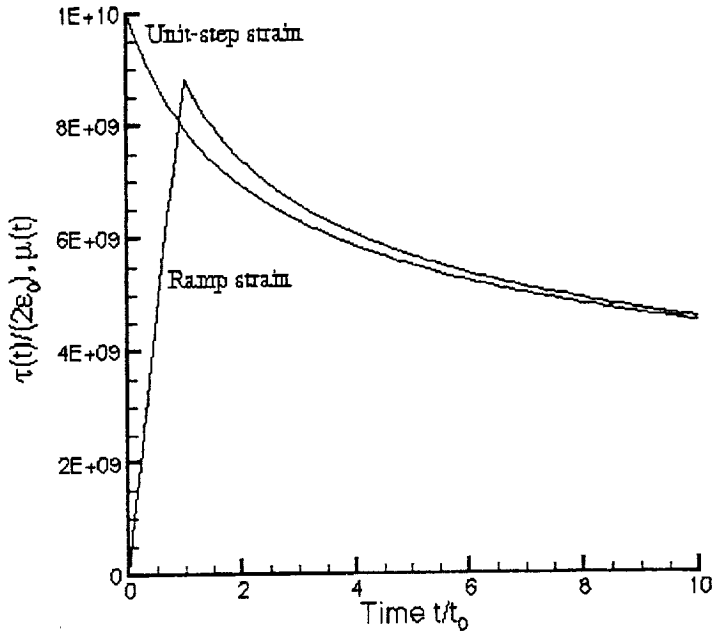

Figure 2. Stress responses for the ramp and step strain histories.

$$m(t) = t\tilde{\mu}(t)$$
$$= \zeta_0 \left\{ \mu_\infty \frac{t}{\zeta_0} + \frac{\mu_0 - \mu_\infty}{1-n} \left[\left(1 + \frac{t}{\zeta_0} \right)^{1-n} - 1 \right] \right\}. \tag{3}$$

This response for a ramp strain is shown in Figure 2 as $\tau(t)/(2\varepsilon_0)$, using the material parameters $\mu_0 = 10^{10}$, $\mu_\infty = 10^7$, $\varsigma_0 = 1$, $n = 1/3$, $t_0 = 1$, and $\dot{\varepsilon}_0 = 0.001$ along with the power law relaxation modulus $\mu(t)$ shown in the same figure.

The two curves approach each other at long times $t \gg t_0$, the difference for this numerical simulation being less than 1.5% once $t > 10t_0$. However, the difference is not negligible ($\sim$ 10%) as $t \to t_0$. To access that time domain for relaxation modulus evaluation, note from Equation (1) that the stress $\tau(t)$ in a ramp history, as evaluated from (1), is

$$\tau(t) = 2\dot{\varepsilon}_0 \int_0^t \mu(\eta)\, d\eta \quad (t < t_0)$$
$$= 2\dot{\varepsilon}_0 \int_0^t \mu(\eta)\, d\eta - 2\dot{\varepsilon}_0 \int_0^{t-t_0} \mu(\eta)\, d\eta \quad (t \geq t_0). \tag{4}$$

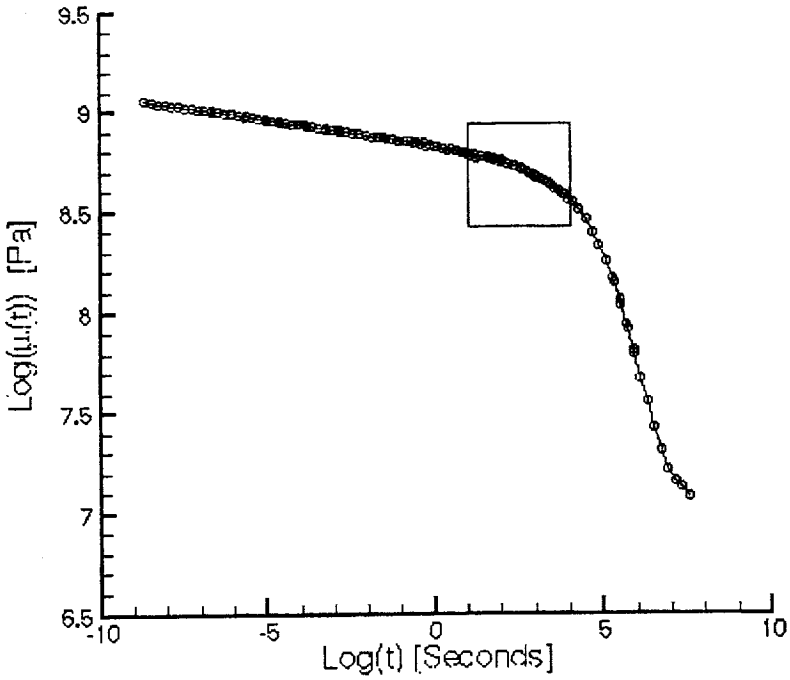

Figure 3. Relaxation master curve in shear for PMMA at 105°C.

Differentiation of (4) gives[1]

$$\mu(t) = \frac{1}{2\dot{\varepsilon}_0}\frac{\mathrm{d}\tau(t)}{\mathrm{d}t} \quad (t < t_0) \tag{5}$$

$$= \mu(t - t_0) + \frac{1}{2\dot{\varepsilon}_0}\frac{\mathrm{d}\tau(t)}{\mathrm{d}t} \quad (t \geq t_0). \tag{6}$$

The relaxation modulus can then be determined with the aid of (6) (and (5)) from the stress data $\tau(t)$ of a ramp strain test by the following sequence:

(i) For $t < t_0$, determine $\mu(t)$ via Equation (5).
(ii) For $t_0 \leq t \leq (1+\alpha)t_0$ with α some sufficiently small number, compute $\mu(t)$ using Equation (6) and the result from step (i).
(iii) For $(1+\alpha)t_0 \leq t \leq (1+2\alpha)t_0$, compute $\mu(t)$ by Equation (6) and the result from step (ii).
(iv) Repeat for $(1+n\alpha)t_0 \leq t \leq (1+(1+n)\alpha)t_0$, $n = 1, 2, \ldots$.
(v) Repeat[2] the same procedure for the subsequent time intervals until, for some time $t \gg t_0$ when the stress response for a ramp strain history (i.e. $\tau(t)/(2\varepsilon_0)$) is very close to the relaxation modulus as illustrated in Figure 2.

Equations (5) and (6) are recursive so that 'backward' computation is also possible. Equation (6) can be written as

$$\mu(t - t_0) = \mu(t) - \frac{1}{2\dot{\varepsilon}_0}\frac{\mathrm{d}\tau(t)}{\mathrm{d}t} \quad (t \geq t_0). \tag{7}$$

At some time $t_* \gg t_0$, $\mu(t_*)$ is assumed to be known. By substituting $\mu(t_*)$ into Equation (7), $\mu(t_* - t_0)$ can be determined for a sequence of times t once the second (correction) term on the r.h.s. has been determined. Repeating this procedure until $t \to 0$ completes the 'backward' computation.

There is a completely analogous formulation for the creep response. This follows from the fact that in liner viscoelasticity convolution integrals describe either relaxation or creep phenomena. Following such an integral representation as given in Equations (4) with the (shear) creep compliance $J(t)$ substituted in place of the relaxation modulus $\mu(t)$ one finds

$$J(t) = \frac{2}{\dot{\tau}_0}\frac{\mathrm{d}\varepsilon(t)}{\mathrm{d}t} \quad (t < t_0) \tag{8}$$

$$= J(t - t_0) + \frac{2}{\dot{\tau}_0}\frac{\mathrm{d}\varepsilon(t)}{\mathrm{d}t} \quad (t \geq t_0) \tag{9}$$

which are expressions equivalent to those in Equations (5) and (6). Accordingly, the earlier results appropriate for ramp-induced relaxation apply to the creep process, also.

3. Data Comparison

It might be suggested that a check on the accuracy of these equations is provided by using an analytical expression for a relaxation modulus to determine the response to a ramp strain input, and then use this 'simulated data' to compute the relaxation modulus for comparison with the original data. It is clear that because Equations (1) and (4–7) are exact, such a computation merely tests the care of the numerical process but not the precision of the estimation process.

To evaluate the recursion formula (7) we thus compute the relaxation modulus in shear from data by Lu (1997) who used thin cylindrical tubes of PMMA in torsion. The glass transition temperature T_g for this material was determined to be 105°C. That data was derived from ramp straining with a rise time of $t_0 = 1$ s, and, while recording the stress every second, the assumption was made that the experimental result represented the relaxation modulus after $t = 10$ s. We use the master relaxation curve, shown in Figure 3, and the raw ramp-induced data from the same reference for the relaxation response at times $t < 10$ s. The (example) raw data in the rectangle of Figure 3 was obtained from experiments conducted at 105°C. We next compute the relaxation modulus by the procedure derived in the previous section and compare it with the master curve.

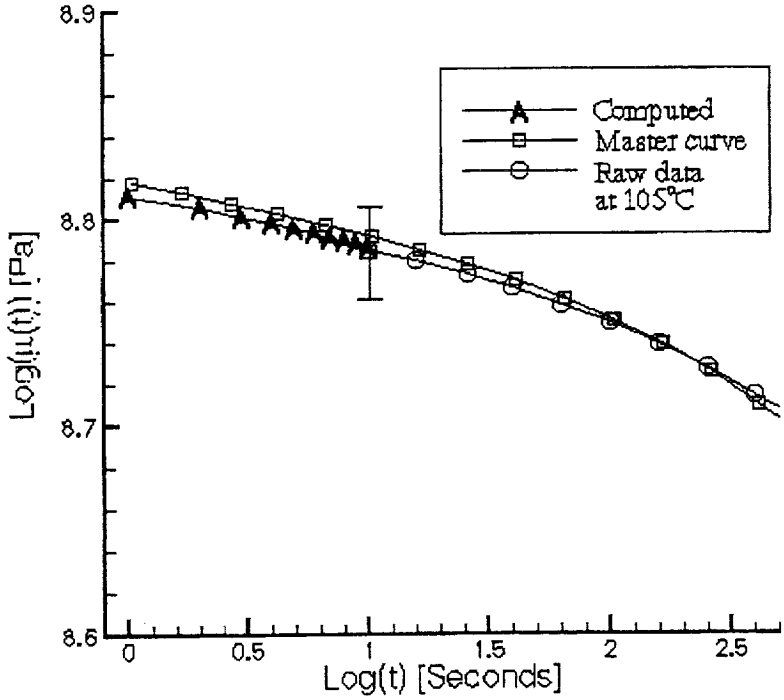

Figure 4. The computed modulus starting from $t_* = 10$ s. Error bar represents ±5% deviation.

Because the stress was not measured during the time between 0 and $t_0 = 1$ s, 'backward' computation applies, starting from a time t_*, according to the following (approximate) relation which employs a time increment 'h' ($h = 1$ s; $\alpha \equiv 1$) in the evaluation of the derivative:

$$\mu(t - t_0) \approx \mu(t) - \frac{\tau(t+h) - \tau(t)}{2\varepsilon_0 h} \quad (t \geq t_0, h = 1 \text{ s}). \tag{10}$$

The computed moduli for the time interval between $t = 1$ and $t = t_* = 10$ s is shown in Figure 4. In view of the error bar representing ±5% one appreciates that the modulus values thus determined fall well within a normal experimental error band. In fact, one may repeat the same computation for a longer interval of $t_* = 150$ s. The corresponding result for that example is shown in Figure 5 with the comparatively same degree of agreement.

To summarize then, a recursion relation for computing the relaxation modulus starting from the ramp time t_0 was derived and applied to experimental data. The procedure functions well even though only a crude approximate differentiation formula was used ($\alpha = 1$) and the time interval h in the formula was not particularly small. The computation of $\mu(t)$ could possibly be made more accurate by measuring the stress in smaller time increments up to the time t_*, because this refinement provides for an improved time derivative of $\tau(t)$ for computation in (8).

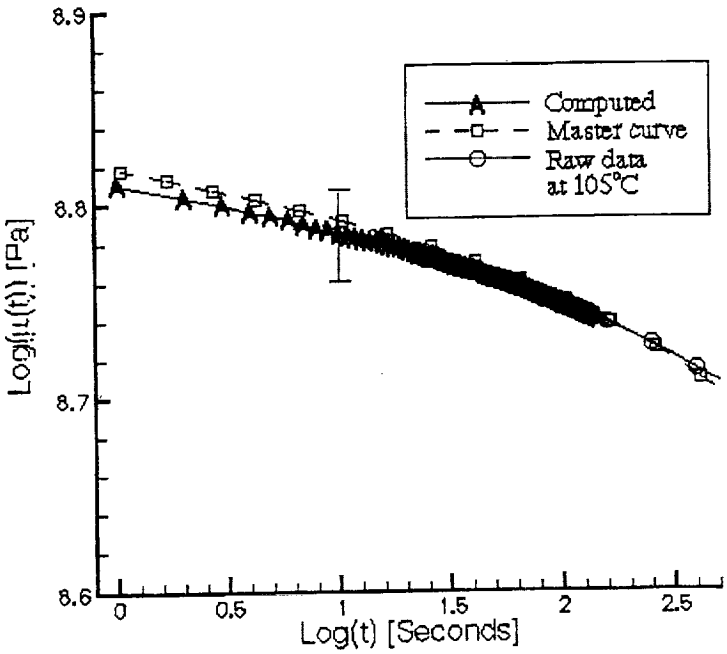

Figure 5. The computed modulus starting from $t_* = 150$ s.

Notes

[1] Note that this approach is an alternate means of deriving relaxation characterization from constant strain rate data as documented by Arenz et al. (1967).

[2] In these steps, differentiation may be performed numerically using an approximate method if the stress is represented only by as a set of discrete values. On the other hand, it may be readily feasible to fit a function to the stress data and perform the differentiation analytically.

References

Arenz, R.J., Ferguson, C.W. and Williams, M.L., 'The mechanical and optical characterization of a Solithane 113 composition', *Experimental Mechanics* **7**, 1967, 183–187.

Lu, H., 'Nonlinear thermo-mechanical behavior of polymers under multiaxial loading', Ph.D. Thesis, Caltech, Pasadena, CA, 1997.